

Applying Raman Spectroscopy to Study Alkali-Silica Reaction Gels

PUBLICATION NO. FHWA-HRT-20-042

JUNE 2020



U.S. Department of Transportation
Federal Highway Administration

Research, Development, and Technology
Turner-Fairbank Highway Research Center
6300 Georgetown Pike
McLean, VA 22101-2296

FOREWORD

Alkali–silica reaction (ASR) is one of the various degradation mechanisms affecting the serviceability of concrete transportation infrastructure in the United States. Despite awareness of this problem since 1940, lack of important information on the ASR gel structure has hampered developing effective early diagnosis or preventive and mitigation strategies. Essential aspects of the ASR mechanism, such as the roles of calcium and aluminum and how the composition of produced gel affects swelling properties in the concrete, can be better understood with an efficient technique to probe the structure of the amorphous ASR gel. The research presented in this report explores the possibility of using Raman spectroscopy as a tool to investigate the structure of ASR gels. Raman spectroscopy provides a simple, powerful method to gain important structural information on ASR gels that could benefit both fundamental research and forensic investigation of concrete. The results of this work may benefit those interested in improving their understanding of the ASR mechanism to develop better test methods or mitigation or repair strategies, including State transportation departments, researchers, and design consultants.

Cheryl Allen Richter, Ph.D., P.E.
Director, Office of Infrastructure
Research and Development

Notice

This document is disseminated under the sponsorship of the U.S. Department of Transportation (USDOT) in the interest of information exchange. The U.S. Government assumes no liability for the use of the information contained in this document.

The U.S. Government does not endorse products or manufacturers. Trademarks or manufacturers' names appear in this report only because they are considered essential to the objective of the document.

Quality Assurance Statement

The Federal Highway Administration (FHWA) provides high-quality information to serve Government, industry, and the public in a manner that promotes public understanding. Standards and policies are used to ensure and maximize the quality, objectivity, utility, and integrity of its information. FHWA periodically reviews quality issues and adjusts its programs and processes to ensure continuous quality improvement.

TECHNICAL REPORT DOCUMENTATION PAGE

1. Report No. FHWA-HRT-20-042	2. Government Accession No.	3. Recipient's Catalog No.	
4. Title and Subtitle Applying Raman Spectroscopy to Study Alkali-Silica Reaction Gels		5. Report Date June 2020	
		6. Performing Organization Code	
7. Author(s) Chandni Balachandran (ORCID: 0000-0001-5198-7448), Jose F. Munoz (ORCID: 0000-0003-2946-9868), and Terence S. Arnold (HRDI-10; ORCID: 0000-0001-5707-6397)		8. Performing Organization Report No.	
9. Performing Organization Name and Address SES Group and Associates LLC 614 Biddle St. Chesapeake City, MD 21915		10. Work Unit No.	
		11. Contract or Grant No. DTFH61-13-D-00007 and DTFH61-17-D-00017	
12. Sponsoring Agency Name and Address Office of Research, Development, and Technology Federal Highway Administration 6300 Georgetown Pike McLean, VA 22101		13. Type of Report and Period Final Report; February 2010–December 2018	
		14. Sponsoring Agency Code HRDI-10	
15. Supplementary Notes The Contracting Officer's Representative was Dennis Sixbey (HRDI-10).			
16. Abstract Alkali-silica reaction (ASR) is a chemical distress mechanism that adversely affects the service life of concrete pavements. Key aspects of the reaction, such as the roles of calcium and aluminum on the structure of the gel and their correlation with swelling properties, have not yet been fully understood owing to the complex reaction mechanism. These problems emphasize the importance of developing analytical techniques, such as Raman spectroscopy, to effectively study ASR products. The research presented in this report explores the possibility of using Raman spectroscopy to provide valuable insight into the structure of ASR gels, both in synthetic systems as well as concrete and mortar samples. This information will aid in better understanding of the mechanism of the reaction and improve repair strategies for damaged structures. The research team used published literature to verify the structural information derived using Raman spectroscopic analysis, thus establishing the validity of the methodology. Increasing alkali content in synthetic ASR gels resulted in depolymerization of the silicate structure, and a strong correlation was observed between the peak position of the most intense band in the low-frequency region and alkali/silica ratio for gels with a composition similar to field ASR gels. Further, an attempt was made to use Raman spectroscopy to characterize ASR gels within concrete and mortar samples, and limitations of applying this technique to probe products within a cementitious matrix were identified. Finally, the study touched on the possibility of using surface-enhanced Raman spectroscopy to improve sensitivity of the technique when applied to concrete samples.			
17. Key Words Raman spectroscopy, alkali-silica reaction gels, silica polymerization, surface-enhanced Raman scattering, silver nanoparticles, concrete		18. Distribution Statement No restrictions. This document is available to the public through the National Technical Information Service, Springfield, VA 22161. http://www.ntis.gov	
19. Security Classif. (of this report) Unclassified	20. Security Classif. (of this page) Unclassified	21. No. of Pages 81	22. Price N/A

Form DOT F 1700.7 (8-72)

Reproduction of completed page authorized.

SI* (MODERN METRIC) CONVERSION FACTORS

APPROXIMATE CONVERSIONS TO SI UNITS

Symbol	When You Know	Multiply By	To Find	Symbol
LENGTH				
in	inches	25.4	millimeters	mm
ft	feet	0.305	meters	m
yd	yards	0.914	meters	m
mi	miles	1.61	kilometers	km
AREA				
in ²	square inches	645.2	square millimeters	mm ²
ft ²	square feet	0.093	square meters	m ²
yd ²	square yard	0.836	square meters	m ²
ac	acres	0.405	hectares	ha
mi ²	square miles	2.59	square kilometers	km ²
VOLUME				
fl oz	fluid ounces	29.57	milliliters	mL
gal	gallons	3.785	liters	L
ft ³	cubic feet	0.028	cubic meters	m ³
yd ³	cubic yards	0.765	cubic meters	m ³
NOTE: volumes greater than 1,000 L shall be shown in m³				
MASS				
oz	ounces	28.35	grams	g
lb	pounds	0.454	kilograms	kg
T	short tons (2,000 lb)	0.907	megagrams (or "metric ton")	Mg (or "t")
TEMPERATURE (exact degrees)				
°F	Fahrenheit	5 (F-32)/9 or (F-32)/1.8	Celsius	°C
ILLUMINATION				
fc	foot-candles	10.76	lux	lx
fl	foot-Lamberts	3.426	candela/m ²	cd/m ²
FORCE and PRESSURE or STRESS				
lbf	poundforce	4.45	newtons	N
lbf/in ²	poundforce per square inch	6.89	kilopascals	kPa
APPROXIMATE CONVERSIONS FROM SI UNITS				
Symbol	When You Know	Multiply By	To Find	Symbol
LENGTH				
mm	millimeters	0.039	inches	in
m	meters	3.28	feet	ft
m	meters	1.09	yards	yd
km	kilometers	0.621	miles	mi
AREA				
mm ²	square millimeters	0.0016	square inches	in ²
m ²	square meters	10.764	square feet	ft ²
m ²	square meters	1.195	square yards	yd ²
ha	hectares	2.47	acres	ac
km ²	square kilometers	0.386	square miles	mi ²
VOLUME				
mL	milliliters	0.034	fluid ounces	fl oz
L	liters	0.264	gallons	gal
m ³	cubic meters	35.314	cubic feet	ft ³
m ³	cubic meters	1.307	cubic yards	yd ³
MASS				
g	grams	0.035	ounces	oz
kg	kilograms	2.202	pounds	lb
Mg (or "t")	megagrams (or "metric ton")	1.103	short tons (2,000 lb)	T
TEMPERATURE (exact degrees)				
°C	Celsius	1.8C+32	Fahrenheit	°F
ILLUMINATION				
lx	lux	0.0929	foot-candles	fc
cd/m ²	candela/m ²	0.2919	foot-Lamberts	fl
FORCE and PRESSURE or STRESS				
N	newtons	2.225	poundforce	lbf
kPa	kilopascals	0.145	poundforce per square inch	lbf/in ²

*SI is the symbol for International System of Units. Appropriate rounding should be made to comply with Section 4 of ASTM E380. (Revised March 2003)

TABLE OF CONTENTS

CHAPTER 1. INTRODUCTION, OBJECTIVES, AND APPROACH	1
Introduction.....	1
Research Objectives.....	1
Research Approach.....	2
Research Significance	2
Outline of Report	3
CHAPTER 2. LITERATURE REVIEW	5
Introduction.....	5
Raman Spectroscopy of Crystalline Phases in Concrete.....	5
Anhydrous Cement Phases	5
Sulfates.....	6
Hydroxides.....	8
Carbonates.....	8
Grey Cementitious Materials	9
Raman Spectroscopy of Glassy Phases	9
High-Frequency Region (800–1,200 cm ⁻¹)	10
Low-Frequency Region (400–700 cm ⁻¹).....	10
Raman Spectroscopy of Amorphous Phases in Concrete	11
Advantages of Using Raman Spectroscopy to Study ASR.....	14
Limitations of Raman Spectroscopy—Fluorescence	15
SERS.....	16
CHAPTER 3. EXPERIMENTAL PROGRAM	19
Introduction.....	19
Materials and Samples	19
Synthetic ASR Gels	19
Accelerated ASR Sample.....	22
SERS Nanoparticle Suspension	25
Analytical Techniques	26
Raman Spectroscopy.....	26
Fourier Transform Infrared Spectroscopy	28
ICP Spectroscopy.....	28
TGA	28
XRD	28
SEM–EDS.....	28
CHAPTER 4. RESULTS AND DISCUSSION.....	29
Introduction.....	29
General Characterization of Synthetic ASR Gels.....	29
Normal Dispersive Raman Spectroscopy of Synthetic ASR Gels.....	30
Raman Spectroscopy of Synthetic ASR Gels	30
High-Frequency Region (800–1,200 cm ⁻¹)	36
Low-Frequency Region (400–700 cm ⁻¹).....	38
Comparison of Raman Spectroscopic Data to NMR data	41

Normal Dispersive Raman Spectroscopy of ASR Samples and Cement Paste	44
Possible Challenges in Using Raman Spectroscopy as a Diagnostic Technique	46
SERS of Cement Paste.....	47
Characterization of Ag Nanoparticle Suspension	47
Influence of Surface Deposition of Ag Nanoparticle Suspension in Raman Signal.....	48
Application of SERS on Cementitious Materials	50
CHAPTER 5. SUMMARY, CONCLUSIONS, AND RECOMMENDATIONS.....	55
Summary.....	55
Conclusions and Recommendations.....	55
APPENDIX. MORPHOLOGY AND CHEMICAL COMPOSITION OF THE	
SYNTHETIC ASR GELS	59
REFERENCES.....	63

LIST OF FIGURES

Figure 1. Graph. Relationship between the position of the most prominent peak in the Raman spectra (high-frequency region) of K/Na silicate glasses with varying M_2O/SiO_2 molar ratios. ⁽⁶⁾	10
Figure 2. Graph. Relationship between the position of the most prominent peak in the Raman spectra (low-frequency region) of K silicate glasses with varying M_2O/SiO_2 molar ratios. ⁽⁶⁾	11
Figure 3. Graph. Relationship between the position of the most prominent peak in the Raman spectra (low-frequency region) of synthetic C-S-H with varying CaO/SiO_2 molar ratios. ⁽³⁴⁾	13
Figure 4. Graph. Relationship between the position of the most prominent peak in the Raman spectra (high-frequency region) of synthetic C-S-H with varying CaO/SiO_2 molar ratios. ⁽³⁴⁾	13
Figure 5. Graph. Raman frequency regions of interest for synthetic C-S-H and ASR gels. ^(34,44)	15
Figure 6. Chart. Raman spectrum of 2-week-old cement paste exhibiting fluorescence. ⁽⁴³⁾	16
Figure 7. Schematic. Ion-exchange column used to produce silicic acid sol for preparing the synthetic ASR gels.	20
Figure 8. Schematic. Procedure for preparing synthetic ASR gels.....	21
Figure 9. Photos. Fresh fracture of samples used to collect Raman spectra of ASR gels.	23
Figure 10. Photo and Chart. Example of void in sample AS1 containing a deposit of ASR gel and the corresponding Raman spectrum collected.	24
Figure 11. Diagram. Synthesis of the suspension of Ag nanoparticles and its surface deposition over cementitious samples for SERS characterization.	25
Figure 12. Charts. Example curve fitting of the representative spectrum of Na gel.....	27
Figure 13. Charts. Raman spectra for synthetic alkali silica gels.	32
Figure 14. Charts. Principal diffraction peaks of carbonate phases in the x-ray diffractograms of synthetic alkali silica gels.	38
Figure 15. Graph. Relationship between the position of the most prominent peak in the Raman spectra (low-frequency region) and the alkali/silica ratio for Na and K gels and for K silicate glasses. ⁽⁶⁾	40
Figure 16. Graph. Relationship between the position of the peak linked to Q^3 silicate sites and the alkali/silica ratio for Na and K gels.	41
Figure 17. Graph. Relationship between the fraction (percentage) of Q^1 , Q^2 , Q^3 , and Q^4 silicate sites determined by the ^{29}Si MAS NMR and alkali/silica ratio for Na gels. ⁽⁴⁶⁾	42
Figure 18. Charts. Relationship between the normalized intensity of Q^1 , Q^2 , Q^3 , and Q^4 peaks in the low-frequency region and the alkali/silica or Ca/Si ratio in synthetic alkali silica gels.	44
Figure 19. Chart. Low-frequency region of Raman spectra of gels from accelerated ASR samples.	45
Figure 20. Chart. UV-Vis absorption spectra of Ag nanoparticle suspension with respect to time and suspension concentration.....	47
Figure 21. Micrograph. SEM micrograph of a Ag nanoparticles.	48

Figure 22. Micrographs and chart. Correlation between suspension deposition (SEM micrograph) and peaks in Raman spectrum of aluminum surface coated with varying concentrations of Ag nanoparticle suspension.	50
Figure 23. Charts. Dispersive Raman spectrum of hydrated OPC samples before and after SERS application.....	51
Figure 24. Chart. SERS spectra of OPC with 10% silica fume (water/cementitious-material ratio = 0.45) after 4 d of hydration collected using 785- and 532-nm lasers.	52
Figure 25. Charts. Spectral interference from a Ag nanoparticles on 7-day-old hydrated cement paste.	54
Figure 26. Micrographs. SEM image and EDS elemental maps of NS1 gel.	60
Figure 27. Micrographs. SEM image and EDS elemental maps of KS2 gel.	61
Figure 28. Micrographs. SEM image and EDS elemental maps of NCS1 gel.	62

LIST OF TABLES

Table 1. Peak positions of anhydrous cement phases (laser wavelengths at 514, 514.5, and 632 nm). ^(12,14)	6
Table 2. Peak positions of sulfate phases in cementitious materials (laser wavelength at 632 nm). (See references 12, 14, 25, and 33.).....	7
Table 3. Peak positions of sulfate phases in cementitious materials (laser wavelength at 514 nm). ⁽¹⁴⁾	7
Table 4. Peak positions of sulfate phases in cementitious materials (laser wavelength at 785 nm). ⁽³²⁾	8
Table 5. Raman peak positions of calcium carbonate polymorphs in cementitious materials (laser wavelength at 782 nm). (See references 12, 14, 34, 36.)	9
Table 6. Targeted chemical composition of the synthetic ASR gels.	22
Table 7. Chemical composition, carbonation and moisture content of the synthetic ASR gels.	30
Table 8. Positions (cm^{-1}) and assignments of the principal vibrational bands in Raman spectra of Na gels. (See references 6, 70, 79–81, 83, and 84.)	33
Table 9. Positions (cm^{-1}) and assignments of the principal vibrational bands in Raman spectra of K gels. (See references 6, 70, 79–81, 83, and 84.)	34
Table 10. Positions (cm^{-1}) and assignments of the principal vibrational bands in Raman spectra of Na-Ca gels. (See references 6, 70, 79–81, 83, and 84.).....	35
Table 11. Positions (cm^{-1}) and assignments of the principal vibrational bands in the low-frequency region of Raman spectra of gels from accelerated ASR samples. ^(6,80,81)	45
Table 12. Characteristic Raman bands and assignments of the Ag nanoparticle suspension. ⁽⁹⁰⁾	48
Table 13. Characteristic Raman regions of hydrated OPC sample.....	52

LIST OF ABBREVIATIONS

Acronyms

ASR	alkali–silica reaction
EDS	energy-dispersive x-ray spectroscopy
FHWA	Federal Highway Administration
FTIR	Fourier transform infrared
ICP	inductively coupled plasma
MAS	magic-angle spinning
NIR	near-infrared
NMR	nuclear magnetic resonance
OPC	ordinary portland cement
SAFETEA-LU	Safe, Accountable, Flexible, Efficient Transportation Equity Act: A Legacy for Users
SB	symmetrical bending
SEM	scanning electron microscopy
SERS	surface-enhanced Raman spectroscopy
SS	symmetric stretching
TGA	thermogravimetric analysis
UV-Vis	ultraviolet–visible
WC	white cement
XRD	x-ray diffraction

Symbols

Ag	silver
Au	gold
C ₂ S	dicalcium silicate
C ₃ A	tricalcium aluminate
C ₃ S	tricalcium silicate
C ₄ AF	tetracalcium aluminoferrite
Ca	calcium
CaO	calcium oxide
Ca(OH) ₂	calcium hydroxide
CaSO ₄	calcium sulfate
CO ₃ ²⁻	carbonate ion
C-S-H	calcium silicate hydrate
H	hydrogen
HCl	hydrochloric acid
K	potassium
KOH	potassium hydroxide
Na	sodium
NaOH	sodium hydroxide
O	oxygen
OH ⁻	hydroxyl ion
Si	silicon
SiO ₂	silicon dioxide

SiO_4
 SO_4^{2-}

silicate
sulfate ion

CHAPTER 1. INTRODUCTION, OBJECTIVES, AND APPROACH

INTRODUCTION

Alkali–silica reaction (ASR) is one of the various degradation mechanisms affecting the serviceability of concrete transportation infrastructure in the United States. This deleterious process involves a reaction between the siliceous phases present in some aggregates and the hydroxyl ions in the pore solution of concrete to form ASR gel. This reaction product can absorb moisture and expand, resulting in cracking of the concrete. Visual manifestations of ASR damage include cracking (typically in a map cracking pattern in unrestrained surfaces), deformation and displacement of structural elements due to expansion, pop outs, and gel exudation.⁽¹⁾ The diagnosis of ASR based on visual symptoms alone is often inadequate and must be corroborated with laboratory investigations of cores extracted from the field. The presence of ASR gel in affected concrete indicates ASR distress.⁽²⁾

The extent of the ASR problem affecting the Nation’s concrete transportation infrastructure motivated the approval of the Safe, Accountable, Flexible, Efficient Transportation Equity Act: A Legacy for Users (SAFETEA-LU) by Congress in 2006.⁽³⁾ SAFETEA-LU has the aim of developing and deploying techniques to prevent and mitigate ASR in concrete infrastructures. The Federal Highway Administration (FHWA) launched the ASR Development and Deployment Program in response to the new legislation. The program proposed four main areas of work to address the problem of ASR, the development of a testing and evaluation protocol being one of them.⁽³⁾

Additionally, the ASR Development and Deployment Program identified the lack of a full understanding of the ASR mechanism as one of factors hindering the development of more effective tools to identify, evaluate, and limit the extent of deleterious expansion.⁽⁴⁾ Key aspects of the mechanism, such as a deeper understanding of the structure of the ASR gel and the relationship between the structure of the gel and chemical composition, have not received much attention by the research community. The use of effective analytical techniques to study ASR gel is thus of utmost importance to address these knowledge gaps.

The research presented in this report explores the possibility of using Raman spectroscopy to study ASR. As a research tool, Raman spectroscopy can provide valuable insight into the structure of the ASR gel, which in turn will aid in better understanding the mechanism of the reaction and improve repair strategies for damaged structures.⁽⁵⁾ Further, the availability of portable instrumental configurations of Raman spectrometers opens the door to the possibility of developing a diagnostic tool that can be deployed in the field for identifying ASR gel.

RESEARCH OBJECTIVES

Raman spectroscopy, with its ability to probe amorphous as well as crystalline materials, is a powerful tool for analyzing concrete or cementitious materials. Over the years, Raman spectroscopy has been applied to characterize various anhydrous cement phases, hydration products, and some secondary cementitious materials, but it has not yet been applied in the area of ASR research. Raman spectroscopy could potentially be a useful technique to characterize ASR gels, especially since it has been used extensively to study similar amorphous materials,

such as silicate melts and glasses.⁽⁶⁾ Therefore, the broad objective of this research effort was to explore the feasibility of using Raman spectroscopy as a fast and easy tool to study the structure of ASR products and develop an understanding of the type of information obtained. A summary of the main objectives of this research are as follows:

- Develop a protocol to analyze ASR products using Raman spectroscopy. This protocol includes spectral interpretation, limitations of the technique, and possible methods to improve sensitivity of the technique.
- Use Raman spectroscopy to establish the relation between chemical composition of the gel and structure/silicate polymerization.

RESEARCH APPROACH

The research presented in this report explores the feasibility of using Raman spectroscopy to study ASR gels, both in synthetic systems as well as concrete and mortar samples, and demonstrates the type of structural information that can be easily deduced using this technique. One of the main challenges of applying Raman spectroscopy to concrete materials research is the inherent fluorescence, which obscures important spectral details, associated with these materials. Considering this limitation and the complex nature of the heterogeneous cementitious matrix, a series of synthetic ASR gels of controlled chemical composition was used to develop a protocol to analyze ASR products using Raman spectroscopy. The structural information derived using Raman spectroscopic analysis was verified from published literature, thus establishing the validity of the methodology. Following this, the research team used Raman spectroscopy to characterize ASR gels within concrete and mortar samples, and limitations of applying this technique to probe products within a cementitious matrix were identified. Finally, the study touched on the possibility of using surface-enhanced Raman spectroscopy (SERS) to improve the sensitivity of the technique when applied to concrete samples.

RESEARCH SIGNIFICANCE

Despite the significant gain in knowledge since 1940 when Thomas Stanton identified the mechanism of ASR, the role that elements like calcium and aluminum play on the structure of the gel and its correlation with swelling properties has not been fully understood.⁽⁷⁾ The heterogeneous nature of ASR products and pore solution composition, which change with time, are additional problems when it comes to addressing this knowledge gap. These problems emphasize the importance of developing analytical techniques like Raman spectroscopy to effectively study ASR gel. Although techniques like nuclear magnetic resonance (NMR) spectroscopy can provide important information regarding silica polymerization of ASR gel, Raman spectroscopy can provide the same information in a much easier manner with the added advantage of the capability of mapping the location of gel within the sample matrix.

Unfortunately, the application of Raman spectroscopy to study gel-like phases in cementitious materials is predominantly limited to calcium silicate hydrate (C-S-H) and nonexistent for ASR gels. Thus, the research presented in this report is instrumental for setting up an analytical protocol to interpret Raman spectra of ASR gels to obtain key silicate polymerization information. The developed analytical protocol includes a curve-fitting approach to resolve two

characteristic broad peaks in Raman spectra of ASR gel into component bands that, in turn, can be used to deduce important structural information.

The availability of portable instrumental configurations of Raman spectrometers opens the door to the possibility of developing a diagnostic tool that can be deployed in the field. The fiber optic probe of a portable Raman spectrometer can focus a laser beam into cracks of ASR-damaged concrete and potentially collect the Raman signal of gel deposits. The recent advent of SERS-active fiber optic probes presents a promising avenue to abate current inherent fluorescence associated with the cementitious matrix surrounding the area of interest, thus allowing for early detection of ASR gel.^(8,9)

OUTLINE OF REPORT

This report is divided into 5 chapters. Chapters 1 and 2 provide an introduction and literature review covering a general overview of the application of Raman spectroscopy in concrete research with special emphasis on the characterization of amorphous phases. Chapter 3 presents a detailed description of the experimental program followed in this study. Chapter 4 contains the results of the study and an in-depth discussion, and chapter 5 presents the main conclusions and recommendations taken from the study.

CHAPTER 2. LITERATURE REVIEW

INTRODUCTION

In 1976, John Bensted first applied Raman spectroscopy to characterize various anhydrous cement phases, hydration products, and some secondary cementitious materials.⁽¹⁰⁾ Initially, Raman spectroscopy was introduced as a complimentary technique to validate infrared band assignments.⁽¹¹⁾ Unlike infrared spectroscopy, the Raman signal is much less sensitive to moisture and, hence, an interesting method to study cementitious materials in situ with minimum sample preparation.

Despite the clear advantages over infrared with respect to sample preparation, the application of Raman spectroscopy to concrete materials was scarce due to technical limitation.⁽¹²⁾ The introduction of Fourier transform Raman spectroscopy and improved laser power, more efficient spectrometers, and faster acquisition times allowed for continuing the pioneering work of Bensted.^(12,13) With the advancement of technology, the application of Raman spectroscopy in concrete materials research has found a renewed interest among the scientific community. The purpose of this chapter is to provide an overview of the multiple applications of Raman spectroscopy to study concrete. The versatility of this spectroscopy technique, allowing for multiple combinations of laser systems and filter units for signal enhancement, expands the possibilities to analyze various crystalline and amorphous phases present in concrete.

RAMAN SPECTROSCOPY OF CRYSTALLINE PHASES IN CONCRETE

Following Bensted's work, several studies exploring the potential of using Raman spectroscopy to characterize various anhydrous cement phases, hydration products, and some secondary cementitious materials have been published. (See references 10–36, 40–42, and 48.) Working with synthetic mineral phases or hydration products of pure cement phases under a specific laser system solved the inherent limitations of Raman spectroscopy, mainly the weak nature of the Raman effect and its strong competition with fluorescence. Several studies have successfully characterized common anhydrous cement phases, such as tricalcium silicate (C_3S), dicalcium silicate (C_2S), tricalcium aluminate (C_3A), and tetracalcium aluminoferrite (C_4AF) and different crystalline sulfate phases using 514-, 632-, and 785-nm lasers. Raman spectroscopy has also shown a remarkable sensitivity to discern between different carbonate phases, such as calcite, aragonite, and vaterite.

Anhydrous Cement Phases

Raman spectroscopy has been used extensively to study pure anhydrous cement mineral phases. Several published works highlight how the different anhydrous cement phases can be readily distinguished using this powerful technique.^(12,14–20) Table 1 summarizes the major Raman peaks of pure cement minerals as reported in a review paper published by Potgieter et al.⁽¹⁴⁾ Raman spectroscopy has often been applied as a quick and efficient technique to analyze the mineral phases in ordinary portland cement (OPC) clinker.^(21,22) Further, Raman spectroscopy has been used to study the hydration of pure cement phases and hydration kinetics of steel slag.^(23–26) A recent advancement is the growing interest in the use of confocal Raman spectroscopy for applications like studying the hydration of C_3S and weathering of cement.^(27,28)

Table 1. Peak positions of anhydrous cement phases (laser wavelengths at 514, 514.5, and 632 nm).^(12,14)

Wavelength Range (cm ⁻¹)	C ₃ S (cm ⁻¹)			C ₂ S (cm ⁻¹)				C ₃ A (cm ⁻¹)	C ₄ AF (cm ⁻¹)
	Triclinic	WC	OPC	alpha	beta	WC	OPC		
300–500	—	—	—	—	—	—	—	—	311
500–700	518–520 540–542	—	—	—	512–520 535–538 556	522 540 558	—	506–508	—
700–900	809–813 840–848 850–855 880–890	832 845	750 832 845	828 850–864 892	845–852 855–860 896–900	848 860 900	740 848 860	754–761	736
>900	—	—	—	—	972–979 1,084	980	—	—	—

—No data.

WC = white cement.

Sulfates

Sulfate groups have a strong Raman signal, which enables Raman spectroscopy to be used effectively to study gypsum and its various derivatives—the main sulfate phases in cement and its hydrations products. Table 2 through table 4 summarize Raman shifts of gypsum and other sulfate phases in cementitious systems as reported in literature for different laser excitation wavelengths. It is evident from these tables that Raman spectroscopy can clearly distinguish the various sulfate phases. Considering the sensitivity of Raman spectroscopy to sulfate phases, this technique has been applied in a number of studies. Renaudin et al. used Raman microspectroscopy to investigate the structural differences in synthetic ettringite and monosulfate phases.⁽²⁹⁾ Garg et al. effectively applied Raman spectroscopy to follow hydration in OPC and OPC–fly ash systems by tracking the disappearance of gypsum and appearance of ettringite.⁽³⁰⁾ Raman spectroscopy has also been successfully used to identify products of sulfate attack on concrete, such as thaumasite.^(31,32) In fact, Raman spectroscopy can also be used to distinguish ettringite and thaumasite, a task that is usually difficult using traditional analytical techniques like scanning electron microscopy (SEM) and x-ray diffraction (XRD).⁽³²⁾ A study to investigate the feasibility of applying a portable configuration of Raman spectroscopy to monitor sulfate attack has also been published.⁽³³⁾

Table 2. Peak positions of sulfate phases in cementitious materials (laser wavelength at 632 nm). (See references 12, 14, 25, and 33.)

Wavelength Range (cm ⁻¹)	Gypsum (cm ⁻¹)				Ettringite (cm ⁻¹)	Thaumasite (cm ⁻¹)	Monosulfate (cm ⁻¹)
	CaSO ₄ ·2H ₂ O	CaSO ₄ ·½H ₂ O	CaSO ₄ Soluble	CaSO ₄ Insoluble			
300–500	414–415 493–494	438 494	438 498	420 500	347 448–450 547–550	—	360 396 447
500–700	622 618–624 670–676	602 636 676	604 624 678	611 630 679	605–612	658	531 614
700–900	—	—	—	—	—	—	—
>900	1,008–1,010 1,114 1,137–1,138 1,144	1,018 1,132 1,150 1,174	1,020 1,131 1,150 1,172	1,022 1,116 1,134 1,166	988–989 1,114–1,119	990 1,072	983 1,114

—No data.

Table 3. Peak positions of sulfate phases in cementitious materials (laser wavelength at 514 nm).⁽¹⁴⁾

Wavelength Range (cm ⁻¹)	CaSO ₄ ·2H ₂ O (cm ⁻¹)	CaSO ₄ ·½H ₂ O (cm ⁻¹)	CaSO ₄ Soluble (cm ⁻¹)
300–500	494	490	490
500–700	623	630 680	608 628 668 685
700–900	—	—	—
>900	1,008 1,114	1,014 1,152 1,174	1,026 1,105 1,152 1,174

—No data.

Table 4. Peak positions of sulfate phases in cementitious materials (laser wavelength at 785 nm).⁽³²⁾

Wavelength Range (cm ⁻¹)	Gypsum (cm ⁻¹)	Ettringite (cm ⁻¹)	Thaumasite (cm ⁻¹)
300–500	413 494	449	418 454
500–700	620 672	548 617	658
700–900	—	—	—
>900	1,006 1,083	988 1,083	990 1,071

—No data.

Hydroxides

The hydration of cement results in the formation of a crystalline calcium hydroxide phase called portlandite. The Raman spectrum of portlandite has two main peaks: one at 3,616 cm⁻¹ attributed to the presence of OH⁻ stretching and another at 353 cm⁻¹ due to Ca–O lattice vibrations.⁽¹²⁾ Garg et al. successfully studied the spatial growth of portlandite in OPC and OPC–fly ash pastes by monitoring the evolution of hydroxides using Raman spectroscopy, illustrating the potential applications of this technique.⁽³⁰⁾

Carbonates

Raman spectroscopy is extremely sensitive to carbonate phases and can easily distinguish various calcium carbonate minerals in an easier and more efficient manner when compared to other analytical techniques like XRD and SEM. Table 5 contains a summary of the main calcium carbonate polymorphs that can be expected in carbonated cementitious materials and depicts how the characteristic ν_1 vibrational band can be used to differentiate the various carbonate phases. A number of studies have used Raman spectroscopy to investigate the carbonation of synthetic C-S-H and hydraulic limes.^(23,34–36) Martinez-Ramirez et al. explored the use of micro-Raman spectroscopy to analyze various forms of calcium carbonate at different depths in a carbonated lime mortar.⁽³⁶⁾

Table 5. Raman peak positions of calcium carbonate polymorphs in cementitious materials (laser wavelength at 782 nm). (See references 12, 14, 34, 36.)

Wavelength Range (cm ⁻¹)	Calcite (cm ⁻¹)	Aragonite (cm ⁻¹)	Vaterite (cm ⁻¹)
100–300	205–207	205–207	300
300–500	—	—	—
500–700	712–713	700 + 704 doublet	740 + 750 doublet
700–900	—	—	—
>900	1,080–1,085 1,450	1,080–1,085	1,074 + 1,090 doublet

—No data.

Grey Cementitious Materials

The use of Raman spectroscopy for studying grey cementitious materials has remained fairly limited as a result of fluorescence compounded with weak Raman signals attributed to the parallel Tyndall scattering of fine powders.⁽³⁰⁾ Nevertheless, the concrete materials research community made efforts to find applications for this technique, especially to study crystalline phases, which innately have a stronger Raman signal than amorphous materials. The following sections further elaborate the application of Raman spectroscopy to study anhydrous cement phases and several crystalline hydration products.

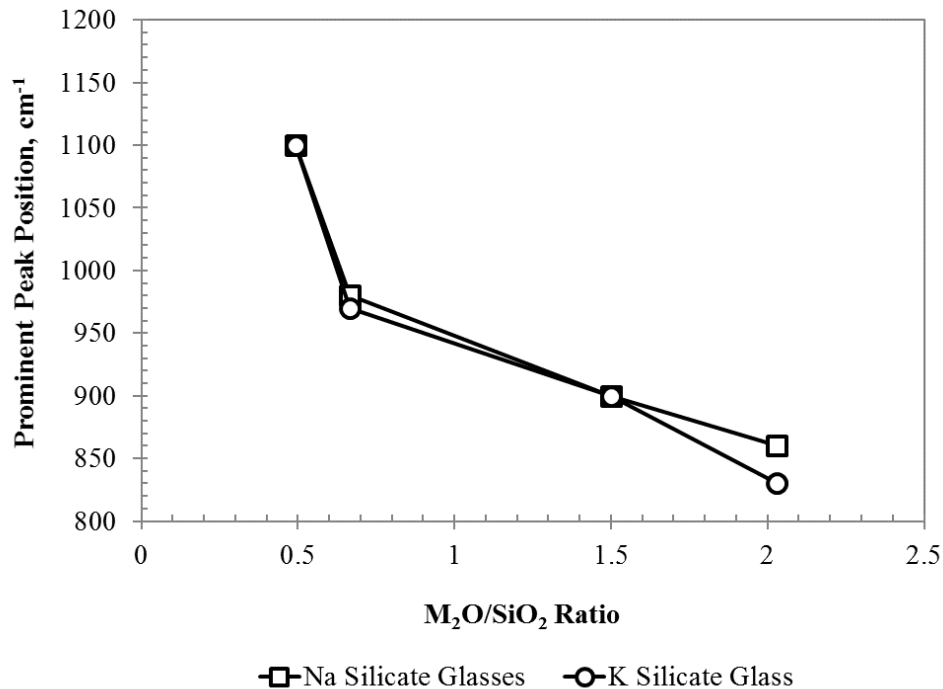
RAMAN SPECTROSCOPY OF GLASSY PHASES

Raman spectroscopy has been used extensively to study silicate melts and glasses primarily due to its ability to probe the structure of these amorphous materials.^(6,37,38) A landmark publication by McMillan provided a thorough review of important Raman spectroscopic studies of alkali and alkaline earth silicate systems.⁽⁶⁾ While there are several publications, some more recent, dealing with Raman spectroscopic studies of alkali silicate glasses, the research team chose the publication by McMillan to elaborate assignments and trends in shifts of specific peaks with changes in composition.⁽⁶⁾ It is important to discuss the trends in Raman data of alkali and alkaline earth glasses because these are very similar to ASR gels, which are the focus of the current study.

In general, there are three regions of interest in the spectra of amorphous glassy material: a high-frequency region between 800–1,200 cm⁻¹; a mid-frequency region between 700–800 cm⁻¹; and a low-frequency region between 400–700 cm⁻¹. The broad envelope in the high-frequency region and low-frequency region contains peaks that are maximized in intensity at certain silicate compositions. The following sections elaborate the specific trends within each of these spectral areas of interest.

High-Frequency Region (800–1,200 cm^{-1})

The high-frequency region of the spectra of alkali silica and alkaline earth silica glasses is attributed to the Si–O symmetric stretching (SS) bands of Q^0 (850 cm^{-1}), Q^1 (900 cm^{-1}), Q^2 ($950\text{--}1,000 \text{ cm}^{-1}$), and Q^3 ($1,050\text{--}1,100 \text{ cm}^{-1}$) silicate sites. Q^0 , Q^1 , Q^2 , Q^3 , Q^4 represent silica tetrahedra with zero, one, two, three, and four bridging oxygens respectively. Figure 1 illustrates the shift in the position of the prominent peak in the broad band in the high-frequency region with alkali silicate glass composition. The data represented in this plot are a compilation of data collected from several relevant publications which have been summarized by McMillan.⁽⁶⁾ Considering the complexity of reporting exact peak positions in sometimes unresolved bands, it is important to emphasize that the main purpose of displaying the data in a plot is merely to display the trend of a shift in the main peak toward lower frequencies with increase in alkali concentrations.



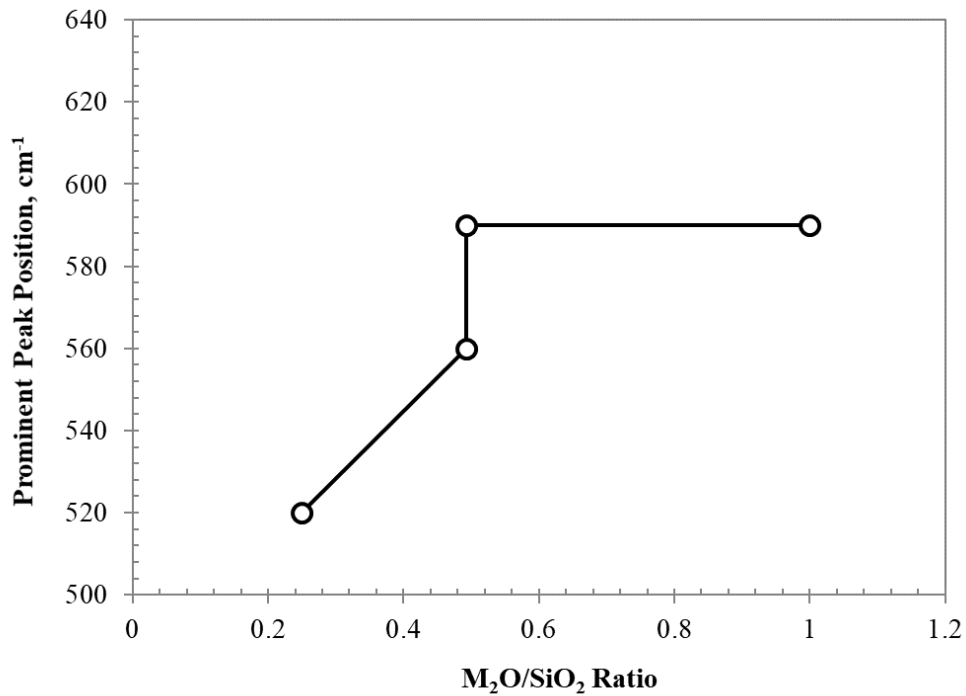
Source: FHWA.
 M_2O = alkali oxide, where M is Na or K.

Figure 1. Graph. Relationship between the position of the most prominent peak in the Raman spectra (high-frequency region) of K/Na silicate glasses with varying M_2O/SiO_2 molar ratios.⁽⁶⁾

Low-Frequency Region (400–700 cm^{-1})

Bands in the low-frequency region of $400\text{--}700 \text{ cm}^{-1}$ are linked to the presence of bridging oxygens or Si–O–Si linkages and are known to vary systematically with changes in composition, which in turn implies changes in the silicate polymerization.⁽⁶⁾ More specifically, bands in the $520\text{--}560 \text{ cm}^{-1}$ range are linked to Q^3 silicate sites, $590\text{--}600 \text{ cm}^{-1}$ range to Q^2 silicate sites, $\approx 700 \text{ cm}^{-1}$ to Q^1 silicate sites, and $\approx 430 \text{ cm}^{-1}$ to Q^4 silicate sites.⁽⁶⁾ Figure 2 illustrates the shift in

the position of the prominent peak in the broad band in the low-frequency region with alkali silicate glass composition.



Source: FHWA.
M₂O = alkali oxide, where M is K.

Figure 2. Graph. Relationship between the position of the most prominent peak in the Raman spectra (low-frequency region) of K silicate glasses with varying M₂O/SiO₂ molar ratios.⁽⁶⁾

RAMAN SPECTROSCOPY OF AMORPHOUS PHASES IN CONCRETE

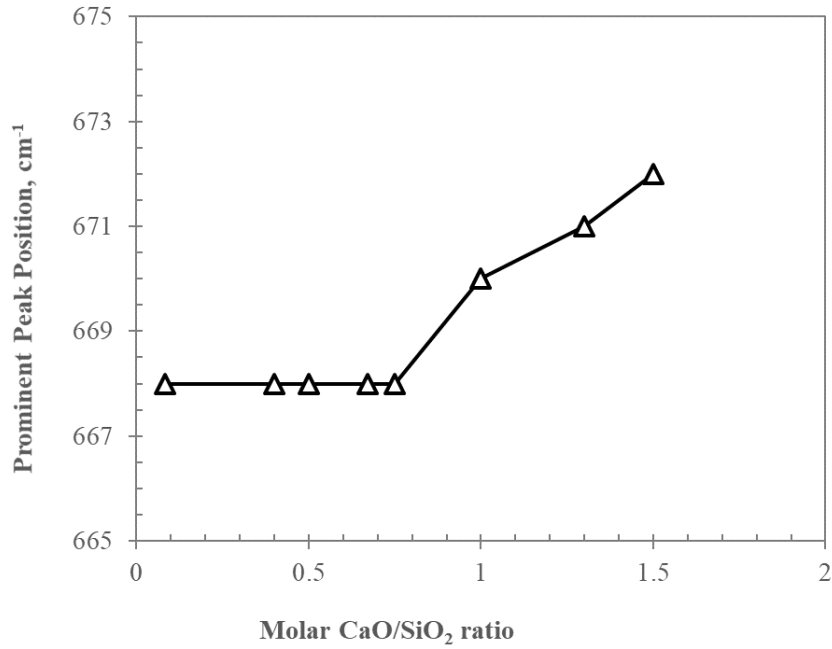
Raman spectroscopy is an ideal technique to explore the structure of amorphous phases. Since the advent of this technique in concrete research, it has been occasionally used to characterize C-S-H, the predominant amorphous hydration product of cement. (See references 12, 14, 34, and 40–42.) Most research efforts focus on characterizing C-S-H, either synthetic or derived from the hydration of white cement (WC) or pure cement phases, due to the fluorescence associated with the analysis of grey cements.^(14,16,19)

Raman spectroscopy can easily provide valuable structural information regarding C-S-H phases, which is consistent with NMR spectroscopic data. In general, Raman spectra of C-S-H phases have three regions of interest: 200–800, 800–1,200; and 3,000–3,800 cm⁻¹. The 200–800 cm⁻¹ frequency region generally comprises peaks assigned to vibrations involving Ca–O polyhedra, internal deformations of Si–O tetrahedra, and symmetrical bending (SB) of Si–O–Si linkages. Of these vibrations, the peaks related to SB vibrations in the 600–700 cm⁻¹ frequency region are the most prominent and important in terms of displaying a systematic shift with changing CaO/SiO₂ ratios. The 800–1,200 cm⁻¹ frequency region is indicative of peaks representing symmetrical C–O stretching in carbonate groups as well as SS of Si–O tetrahedral. As evident in the

low-frequency region, the SS bands also show a progressive shift with varying CaO/SiO₂ ratios. The 3,000–3,800 cm⁻¹ frequency region contains peaks related to O–H stretching vibrations of water molecules and portlandite.

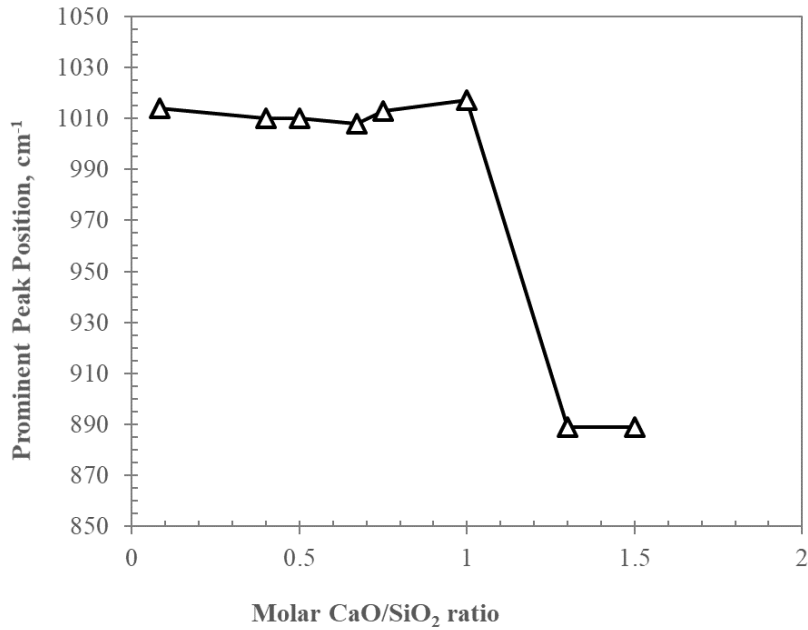
Figure 3 and figure 4 present a closer view of the systematic shifts observed in the SB and SS peaks of C-S-H with changing CaO/SiO₂ ratios based on data from a publication by Garbev et al.⁽⁴¹⁾ This particular study was chosen to emphasize the relationship between the prominent peak position in each Raman spectrum and the chemical composition since the data were collected from fresh C-S-H that was protected from carbonation. C-S-H carbonates rapidly upon exposure to the atmosphere, and the presence of the Raman peaks due to C–O in carbonate groups greatly hinders the clarity of observing shifts in peaks, especially in the SS region.⁽⁴¹⁾ As illustrated in figure 3, in the 600–700 cm⁻¹ frequency region, the prominent peak in the Raman spectra of C-S-H remains more or less constant at 668 cm⁻¹ for gels with CaO/SiO₂ up to 0.8, and then the peak gradually drifts to slightly wavenumbers after CaO/SiO₂ ratios greater than 1. This shift from 668 cm⁻¹ to 672 cm⁻¹ suggests a progressive depolymerization of the silicate structure or narrowing of the Si–O–Si bridging bond angle as a consequence of less coupling of single silicon-bridging oxygen stretching vibrations.

In the high-frequency SS region, as shown in figure 4, the position of the prominent vibrational band remains at around 1,010 cm⁻¹ for C-S-H with CaO/SiO₂ ratios less than 1, following which the prominent peak shifts to lower frequencies of 889 cm⁻¹. The shift in this frequency region is also indicative of depolymerization of the silicate structure with increasing calcium content of the C-S-H. As is clear from figure 3 and figure 4, the position of dominant peaks in the Raman spectra of C-S-H have a correlation with the chemical composition. In other words, Raman spectroscopy is an easy and efficient technique to study the effect of the chemical composition of these phases on the silicate polymerization.



Source: FHWA.

Figure 3. Graph. Relationship between the position of the most prominent peak in the Raman spectra (low-frequency region) of synthetic C-S-H with varying CaO/SiO₂ molar ratios.⁽³⁴⁾



Source: FHWA.

Figure 4. Graph. Relationship between the position of the most prominent peak in the Raman spectra (high-frequency region) of synthetic C-S-H with varying CaO/SiO₂ molar ratios.⁽³⁴⁾

ADVANTAGES OF USING RAMAN SPECTROSCOPY TO STUDY ASR

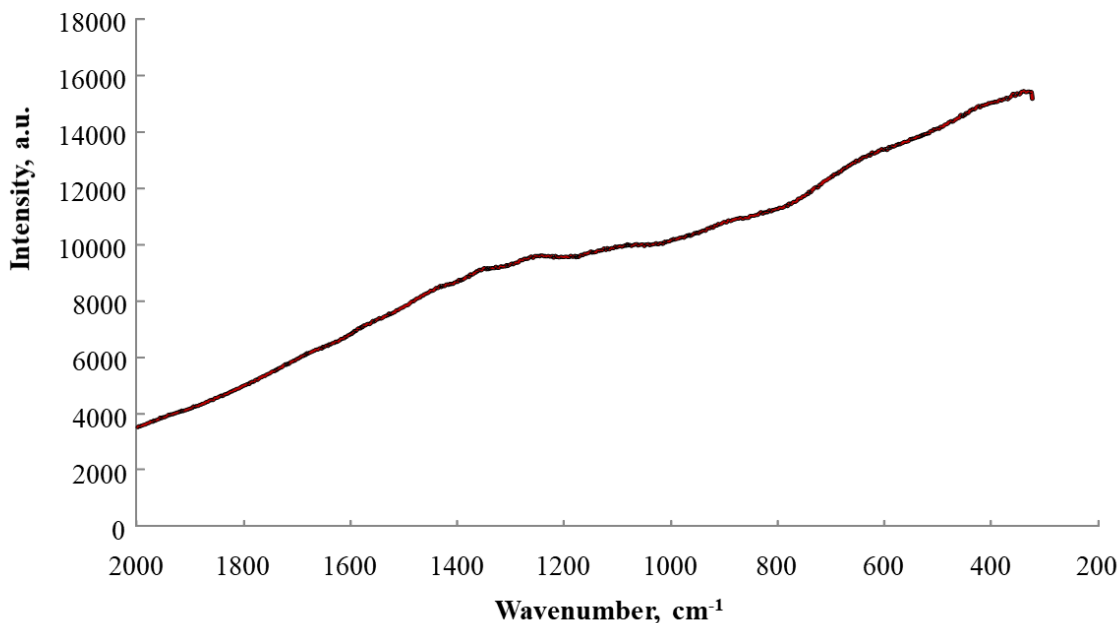
The ability of Raman spectroscopy to probe the structure of amorphous materials makes it an ideal technique to characterize ASR gels. Despite being utilized occasionally in concrete materials research, the potential application of Raman spectroscopy in ASR research has not received substantial interest to date. It has, however, been used extensively to study similar amorphous materials like silicate melts and glasses.^(6,37,38)

Recently, FHWA initiated pioneering work on the application of Raman spectroscopy to study the structure of ASR gels. Several sections of this work have been summarized in a couple publications.^(43,44) As part of this large study, the structures of several synthetic ASR gels were thoroughly characterized using Raman spectroscopy.⁽⁴⁴⁾ It was proved that the trends in silicate polymerization changes with respect to varying ASR gel composition were in close agreement with results from a NMR study on similar synthetic ASR gels. Thus, it was evident that Raman spectroscopy could indeed prove to be a powerful tool to investigate changes in the structure of ASR gels in an easy, nondestructive manner. A subsequent study by Leeman explored the use of Raman microscopy to study ASR gel within cracks in concrete.⁽⁴⁵⁾

Figure 5 shows the Raman frequency regions of interest for the prominent peaks of C-S-H and ASR gels. The red lines denote the approximate expected peak positions in the Raman spectrum of C-S-H based on data collected for synthetic C-S-H from literature.⁽³⁴⁾ The grey areas represent the frequency regions where the prominent Raman bands of ASR gels will appear based on data collected from a range of synthetic ASR gels.⁽⁴⁴⁾ As is clear in figure 5, there is significant overlap between the peaks of C-S-H and ASR gels in the high-frequency region (800–1,200 cm^{-1}). However, in the 520–650 cm^{-1} frequency region, the peaks of ASR gel should appear distinct from peaks of C-S-H. This is an important observation that suggests Raman spectroscopy is indeed an ideal tool to characterize ASR gels given the fact that it can distinguish this gel from C-S-H within a concrete sample.

unhydrated cement, WC, synthetic C-S-H, or hydration of pure cement phases. Unfortunately, this technique has been largely limited to analyzing grey cements due to their high background signal attributed to fluorescence, photoluminescence, multiple scattering, and peak overlap, which in turn obscures important spectral details.⁽¹⁶⁾ These issues, coupled with the fact that Raman scattering of C-S-H is inherently poor, have led to Raman spectroscopy being labeled as potentially unsuitable for studying OPC systems.^(10,16) Figure 6 indicates the broad fluorescent signal in the Raman spectrum of a hydrated cement paste collected using a 785-nm laser.

The exact reasons behind why fluorescence occurs are not entirely clear; some studies claim that the high levels of iron are the culprit.⁽¹⁶⁾ However, a few studies disprove this theory.^(22,49) Other theories, such as defects and interparticle scattering introduced by grinding, have been proposed but have not been able to adequately explain the fluorescent background observed while analyzing most OPCs but not WCs.⁽¹⁶⁾



Source: FHWA.

Figure 6. Chart. Raman spectrum of 2-week-old cement paste exhibiting fluorescence.⁽⁴³⁾

Previous attempts to reduce fluorescence, such as using a Raman microprobe or Fourier transform Raman with near-infrared (NIR) excitation, have resulted in limited success.⁽¹⁷⁻¹⁹⁾ However, a structured fluorescence effect was reported when using NIR excitation for the Raman spectroscopy of OPCs.⁽¹⁹⁾ Newman et al. suggested this phenomenon is linked to the presence of orthosilicates, which progressively decreased as the cement hydrated.⁽¹⁹⁾

SERS

Another method to combat fluorescence is SERS. The SERS phenomenon, first reported in 1974, involves enhancing the Raman signal by many orders of magnitude following the adsorption of analyte molecules on plasmonic nanostructures. In SERS, the molecules of interest are in the

vicinity of a nanostructured metal (i.e., silver (Ag), gold (Au), and copper), which results in an enhancement of their Raman signal. Some studies claim that the enhancement produced by SERS is due to a combination of an electromagnetic and chemical interaction between the nanostructured metal and target molecule.^(50,51)

Since the discovery of SERS, nanospheres of SERS-active metals, principally Ag and Au, have been used extensively in research due to the simplicity of their synthesis and possibility to produce quantitatively size-controlled nanoparticles.⁽⁵⁰⁾ The nanospheres are obtained in a suspension by the reduction of the metal salt with specific chemicals. Later, these suspensions can be easily used to analyze dissolved compounds in aqueous solutions or solid samples (e.g., paints and minerals) when deposited as coatings.⁽⁵²⁻⁵⁸⁾ The key role of the shape and arrangement of the nanostructures in SERS motivated the development of a SERS-active substrate, which produce a more controlled arrangement of the nanostructures.⁽⁵⁰⁾ Improving the aggregation of the nanospheres reduced the frequency of random changes in the intensity of the spectrum produced.⁽⁵⁹⁾ Aside from the production of suspensions of SERS-active metals, alternative methods have been developed to produce different types of SERS-active structures. A common strategy is to coat different materials with SERS-active metals to make them SERS active. An example of this approach is the deposition of Ag films over nanospheres, nanosphere lithography, Ag island films, or infiltration of porous films with SERS-active nanoparticles.^(60,61) The recent advent of SERS-active fiber optic probes presents a promising approach to overcome the problem of fluorescence of cementitious materials when used in field applications.^(62,63)

CHAPTER 3. EXPERIMENTAL PROGRAM

INTRODUCTION

Two types of samples were prepared to explore the feasibility of using Raman spectroscopy to study the structure of ASR gels:

1. A series of synthetic ASR gels of varying alkali/silica and calcium/silica molar ratios was prepared and thoroughly characterized using inductively coupled plasma (ICP) spectroscopy, XRD, and thermogravimetric analysis (TGA). The initial feasibility of Raman spectroscopy to probe the structure of ASR gels was evaluated on these controlled synthetic gel samples.
2. The nature of the Raman spectra collected from the synthetic ASR gels was further validated by collecting the Raman signal of ASR gels in a more realistic environment. Three different methods to produce ASR gels within a cementitious matrix in an accelerated manner were employed. The resulting gels were not only used as examples to validate the interpretation of Raman spectra developed using synthetic gels but also to evaluate the feasibility of detecting ASR gel within a cementitious matrix that is expected to fluoresce.

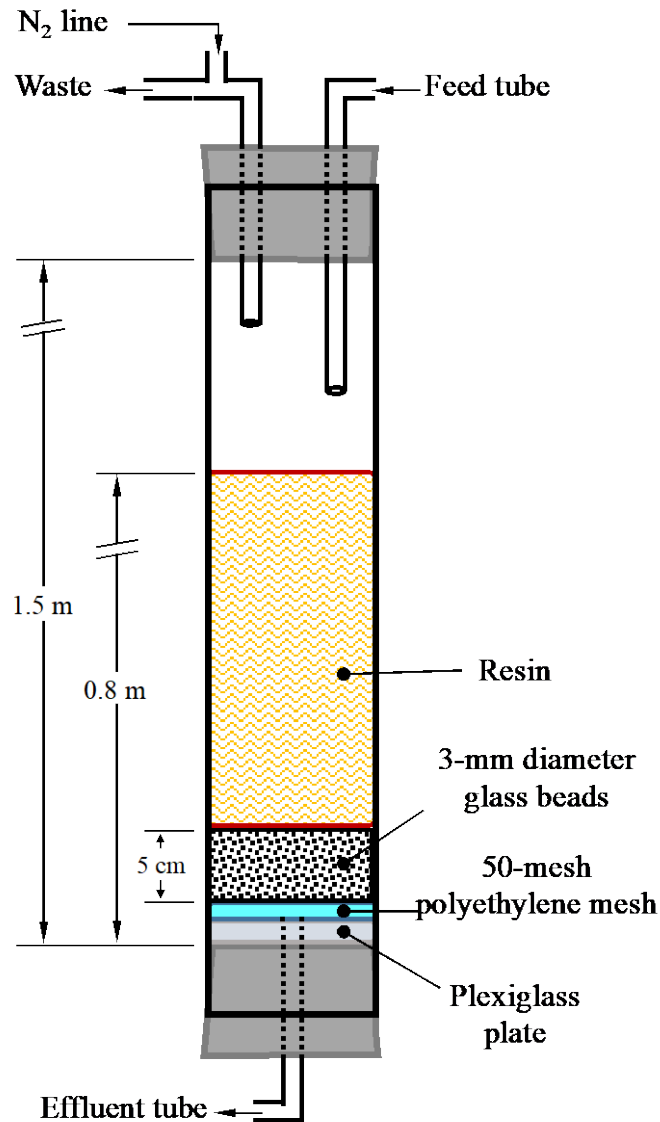
MATERIALS AND SAMPLES

Synthetic ASR Gels

Three series of synthetic ASR gels—sodium silica gels (Na gels), potassium silica gels (K gels), and sodium calcium silica gels (Na-Ca gels)—of controlled composition were produced following a procedure described by Struble et al.⁽⁶⁴⁾ Reagent grade chemicals were used for all the syntheses. In short, the method involved adding controlled amounts of alkalis to a silicic acid sol prepared by ion exchange of a sodium silicate solution followed by vacuum evaporation until constant mass was achieved. The following section provides a detailed description of the protocol.

Ion-Exchange Column

An ion-exchange column was prepared by packing a 1.5-m polyethylene tube with a H⁺ cation-exchange resin up to a depth of 0.8 m, as shown in figure 7. The resin bed, which was a depth of 5 cm, was supported over a 50-mesh polyethylene screen and made up of 3-mm glass beads. The column was provided with an inlet with two openings. One opening was for the tube to feed the sodium silicate solution into the ion-exchange column. The second opening was connected to a tube to collect waste solution from backflushing the column and also to a nitrogen gas purge line. The purpose of bleeding nitrogen into the column was to prevent carbonation during the ion-exchange process of the sodium silicate solution. An outlet was provided at the bottom of the tube to collect either the effluent solution or waste solution during sol preparation and also to pump water up to backflush the column. A peristaltic pump was used to control the flow of sodium silicate solution into the tube and also for pumping water for rinsing and backflushing the column.



Source: FHWA.

Figure 7. Schematic. Ion-exchange column used to produce silicic acid sol for preparing the synthetic ASR gels.

Ion-Exchange Column Operation and Maintenance

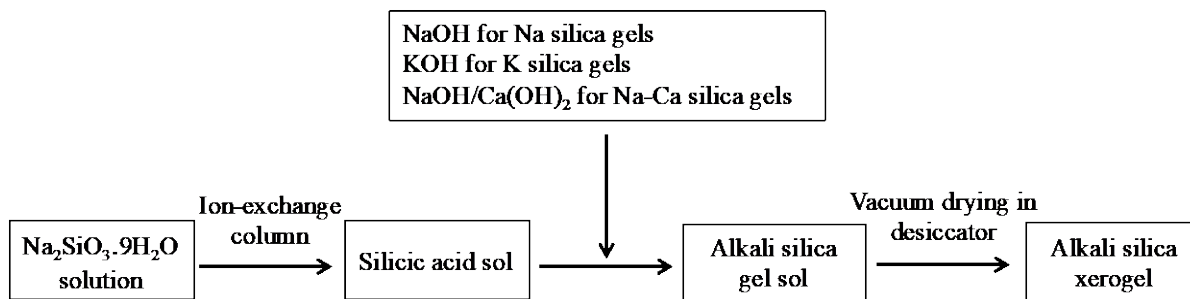
On the day of silicic acid sol preparation, the column was first rinsed with 1 L of deionized water. All water was boiled to remove carbon dioxide. A 0.8-M $\text{Na}_2\text{SiO}_3 \cdot 9\text{H}_2\text{O}$ solution was fed into the ion-exchange column at a flow rate of 30 ml/min. Once the liquid level rose to approximately 10 cm, the outlet valve was opened to a flow rate of approximately 20 ml/min. The first 300 ml of the effluent was discarded, following which the effluent was collected in aliquots of 50 ml until 500 ml of the effluent exited the column. Each of the 50-ml aliquot of effluent collected from 300 to 500 ml was then analyzed in the ICP spectrometer to confirm that only the sol that was completely exchanged was used and that the Si concentration was the same in the feed solution. The resulting silicic acid sol was then processed to make ASR gels as

described in the Ion-Exchange Column section. After collecting the silicic acid sol, the column was rinsed thoroughly with deionized water, backflushed for 10 min and left filled with water. Prior to the next run of the column, the resin was regenerated by passing 2 L of 1-M HCl followed by 30 min of rinsing with water.

Gel Preparation From Silicic Acid Sol

The silicic acid sol collected from the column from 350 to 500 ml of the effluent was combined and used to prepare synthetic ASR gels of varying composition, which is further described in this section and represented in the schematic shown in figure 8. The Na gels were prepared by using a burette to add fixed volumes of a 12.5-N NaOH solution to 50 ml of the silicic acid sol under constant stirring. In a similar fashion, to prepare the potassium silica gels (K gels), 12.5 N of KOH was added, and for the sodium calcium silica gels (Na-Ca gels), a combination of 12.5 N of NaOH and a saturated solution of $\text{Ca}(\text{OH})_2$ was added.

After thoroughly mixing the sol and added solutions, the mixture was transferred into several polyethylene beakers to ensure faster drying. The gels were left to dry under vacuum until constant mass was observed, following which the xerogel samples were transferred into polypropylene storage vials and stored under vacuum in a desiccator to minimize carbonation. The alkali oxide/silica and calcium oxide/silica molar ratios will be referred to as Na/Si, K/Si, and Ca/Si ratios in the rest of this report.



Source: FHWA.

Figure 8. Schematic. Procedure for preparing synthetic ASR gels.

The chemical composition of each synthetic gel was verified using ICP spectroscopy. The xerogels were fused prior to digestion with HCl, following which they were analyzed for elemental composition using ICP spectroscopy. Table 6 summarizes the theoretical Na/Si, K/Si, and Ca/Si ratios of the synthetic ASR gels.

Table 6. Targeted chemical composition of the synthetic ASR gels.

Gel Type	Gel Code	Molar Ratio	
		Target M*/Si	Target Ca/Si
Na	NS1	0.25	0.00
	NS2	0.50	0.00
	NS3	0.75	0.00
	NS4	1.00	0.00
	NS5	2.00	0.00
K	KS1	0.25	0.00
	KS2	0.50	0.00
	KS3	0.75	0.00
	KS4	1.00	0.00
Na-Ca	NCS1	0.50	0.05
	NCS2	0.50	0.10
	NCS3	0.50	0.20
	NCS4	0.50	0.40

*M = Na or K.

NS = Na gel series; KS = K gel series; NCS = Na-Ca gel series.

Accelerated ASR Sample

Raman spectroscopic studies were also conducted on ASR gel samples either produced within or extracted from concrete or mortar samples in which ASR distress was produced under accelerated conditions. These accelerated ASR samples were either obtained from outside sources or prepared at the Turner-Fairbank Highway Research Center. While a detailed Raman characterization of the gel was not the main focus of this part of the study, the aim was to merely gauge the potential of using this technique either as a research or diagnostic tool in samples closer to what can be expected in the field.

ASR Gel From Pyrex Glass

Following the methodology developed by Ostertag et al., mortar bars were prepared with Pyrex glass rods embedded in them, using a nonreactive aggregate and exposed to 1N NaOH at 80 °C.⁽⁶⁵⁾ The expansion of the mortar bars was monitored on a regular basis. After 4 mo of exposure, the mortar bars were stored for another 4 mo, following which they were removed from the soak solution and split open to reveal fresh fracture surfaces, as shown in figure 9. Large portions of the glass rod reacted completely. Deposits of a translucent gel lined voids in the vicinity of the glass rod and also along its path, as illustrated in figure 10-A. The gel was extracted using a spatula and analyzed using Raman spectroscopy. Herein, this gel sample will be referred to as AS1.

ASR Gel From Concrete Prism

Concrete prisms, such as the one shown in figure 9, containing a reactive aggregate (rhyolite from New Mexico) and exposed to 1N NaOH at 38 °C for 1 yr was obtained from an external source.⁽⁶⁶⁾ The concrete prism was split open with a hammer and chisel, and the fresh fracture surface was examined for visible deposits of ASR gel. Suspect samples of gel were analyzed using Raman spectroscopy either in situ or after being extracted. SEM–energy-dispersive x-ray

spectroscopy (EDS) analysis confirmed that the extracted samples were ASR gel of Ca-Si-Na composition. Herein, this gel sample will be referred to as AS2 in the rest of the report.



Source: FHWA.

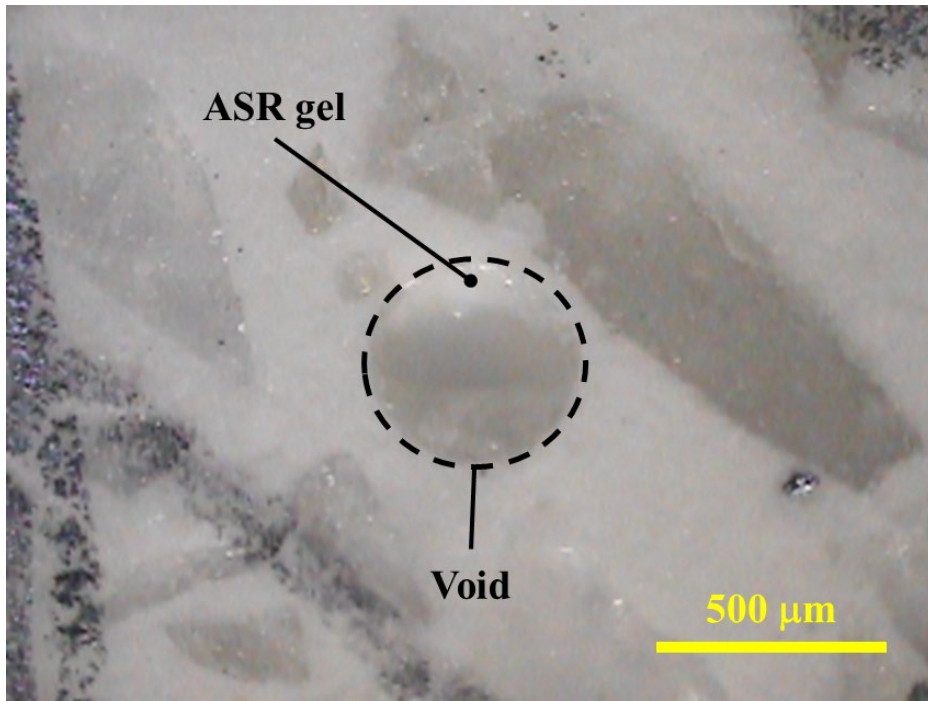
A. Mortar bar of AS1 sample.



Source: FHWA.

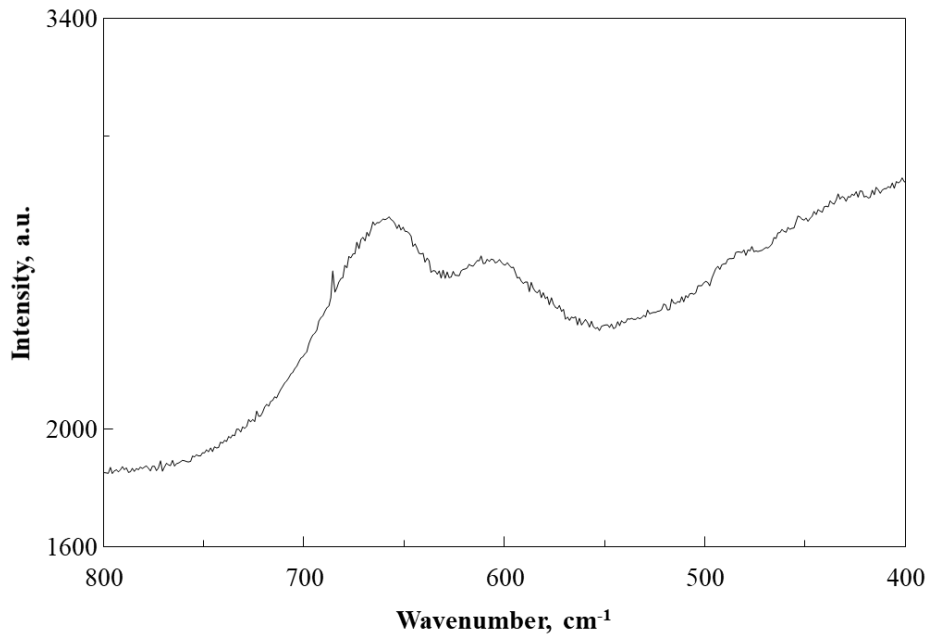
B. Concrete prism of AS2 sample.

Figure 9. Photos. Fresh fracture of samples used to collect Raman spectra of ASR gels.



Source: FHWA.

A. Void in sample AS1 from which a gel was extracted for Raman spectroscopic analysis.



Source: FHWA.

a.u. = arbitrary units.

B. Raman spectrum of ASR gel collected from void shown in figure 10-A.

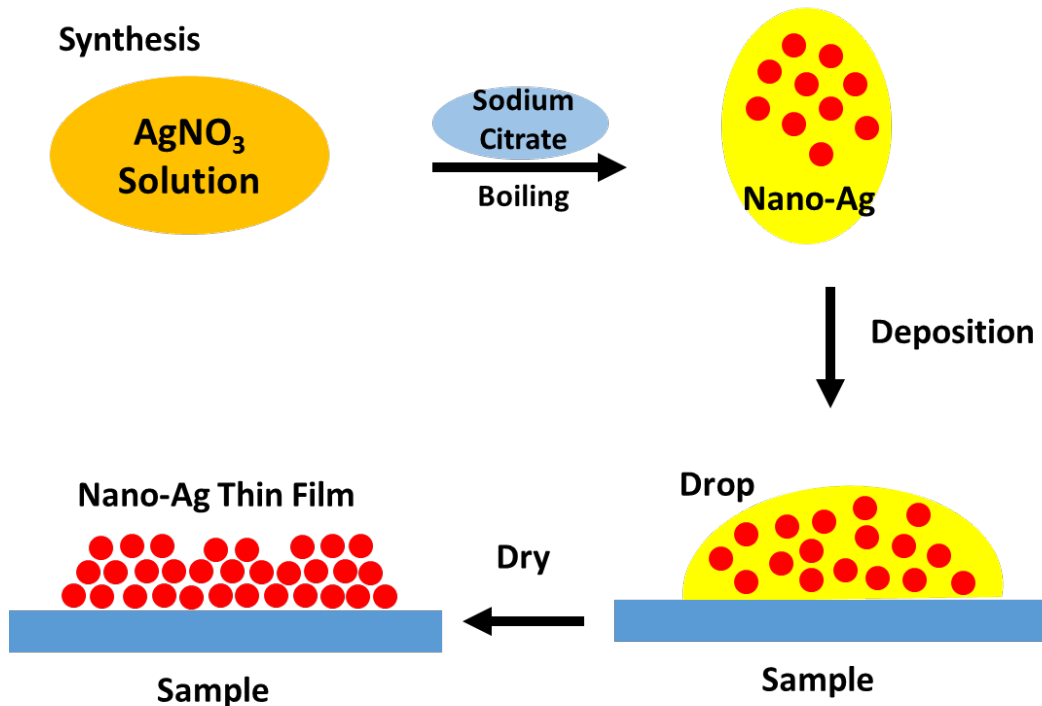
Figure 10. Photo and Chart. Example of void in sample AS1 containing a deposit of ASR gel and the corresponding Raman spectrum collected.

ASR Gel From Mortar Bar

Mortar bars were prepared using a reactive sand (i.e., mixed mineralogy of quartz, chert, and feldspar from El Paso, TX) and high alkali cement as per the specifications of ASTM C 1260 (water/cement ratio = 0.47).⁽⁶⁷⁾ The mortar bars were stored in water at 80 °C for 1 d, following which they were transferred to a 1N NaOH bath at the same temperature. Expansion of the mortar bars was monitored two times a week over a 2-mo period. The mortar bars were allowed to remain in these exposure conditions for 2 mo, following which they were removed from the storage solution and split open to expose fresh fracture surfaces. Gel deposits within large voids were characterized using Raman spectroscopy. Herein, this gel sample will be referred to as AS3.

SERS Nanoparticle Suspension

The SERS material selected for this study were Ag nanoparticles. The research team prepared a suspension of nanoparticles following a method proposed by Lee and Meisel.⁽⁶⁸⁾ The method required the reduction of Ag nitrate with sodium citrate. The Ag nanoparticle suspension was characterized using ultraviolet–visible (UV-Vis) spectrometry and SEM. The UV-Vis absorbance maximum of the nanoparticle suspension was about 420 nm. SERS measurements were obtained by depositing approximately 3 μL of the suspension on the surface of the sample and collecting the Raman spectra after the suspension had dried. Figure 11 is a diagram of the synthesis and subsequent deposition of the Ag nanoparticle suspension on the samples.



Source: FHWA.

Figure 11. Diagram. Synthesis of the suspension of Ag nanoparticles and its surface deposition over cementitious samples for SERS characterization.

ANALYTICAL TECHNIQUES

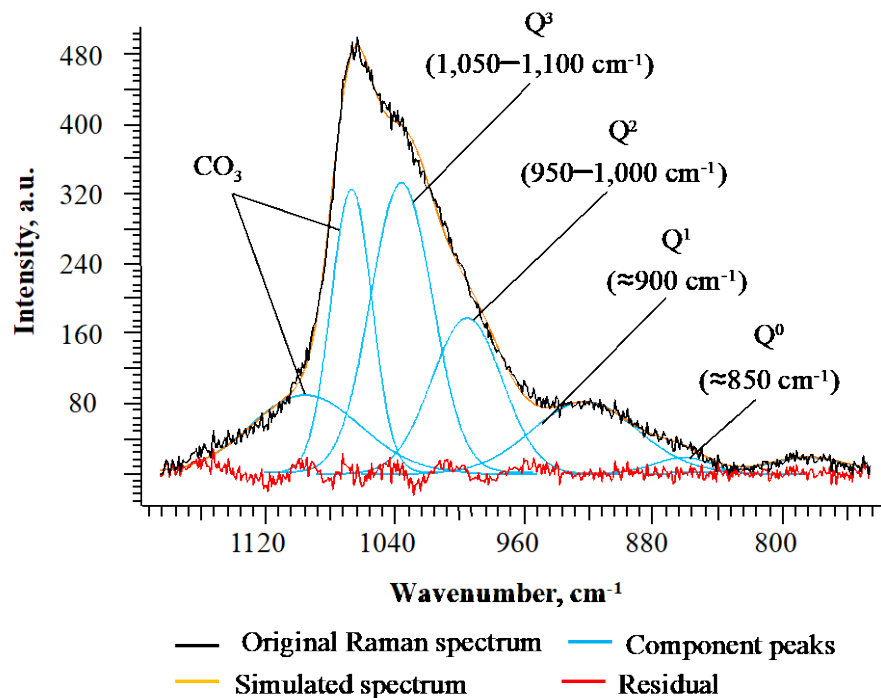
Raman Spectroscopy

The research team collected all Raman spectra in this report using a laser Raman spectrophotometer equipped with two lasers of 532 and 785 nm, three microscope objectives of $\times 20$, $\times 50$, and $\times 100$ magnification, and a charge-coupled device detector. Based on the nature of the sample for analysis, the research team changed the configuration of the spectrophotometer. The specific details of each configuration are described as follows:

- The Raman spectra of the synthetic ASR gel samples were collected using a 532-nm laser operating at 8.8 mW. The Raman data were collected using a $\times 20$ microscope objective and 2 accumulations of exposure time of 120 s.
- The ASR gel in the accelerated ASR samples was analyzed using a 785-nm laser operating at 135 mW. The Raman data were collected using a $\times 100$ microscope objective. The exposure time and number of accumulations were adjusted for every sample to obtain the best signal without saturating the detector.
- The samples coated with SERS particles were characterized using a 785-nm laser operating at 135 mW with a $\times 100$ microscope objective. The exposure time and number of accumulations were adjusted for every measurement to obtain the best signal without saturating the detector.

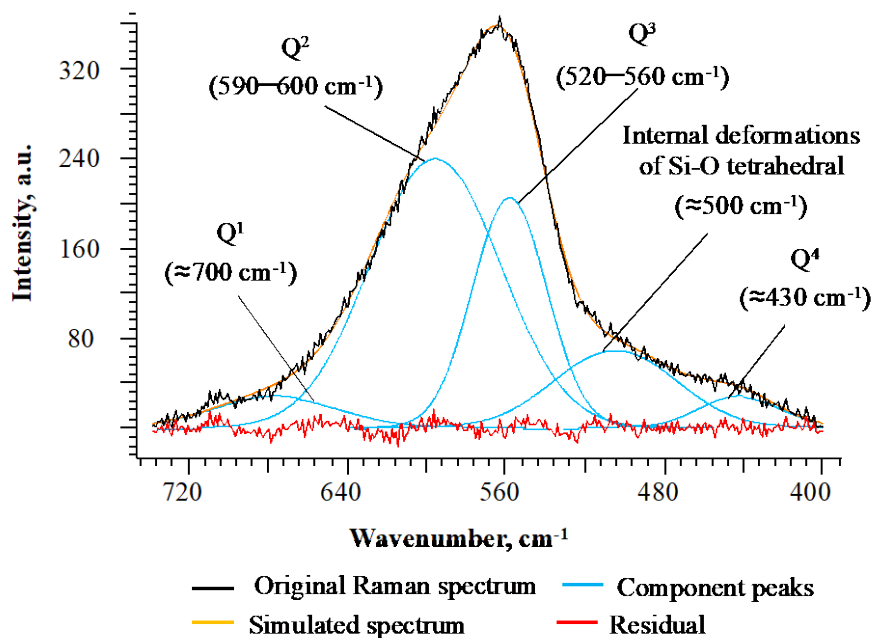
Processing the Raman Spectra of the Synthetic ASR Gels

Broad peaks in the Raman spectra of the synthetic gels were assumed to be due to superimposition of several symmetrical peaks.^(41,69) To derive valuable information from the broad bands of the amorphous gels, all the spectra were processed using a curve-fitting procedure that separated the bands into their component peaks.^(36,69–73) The Raman spectra were normalized, background corrected, and curve fitted assuming Gaussian functions using a spectral processing software.^(69–71) Figure 12 shows an example of the background corrected and curve-fitted spectra for the high- and low-frequency ranges of a representative Na gel. An important limitation of curve fitting is that there is no unique solution to achieve a good fit. The curve fitting approach adopted in this study was validated by the fact that the silica polymerization information derived from band assignments based on curve fitting was in agreement with previous results of a Raman spectroscopic investigation of amorphous silica materials and, more specifically, of similar synthetic ASR gels using solid-state NMR data.^(71,74)



Source: FHWA.
 a.u. = arbitrary units.

A. Example curve fitting of the representative spectrum of Na gel in the high-frequency region.



Source: FHWA.
 a.u. = arbitrary units.

B. Example curve fitting of the representative spectrum of Na gel in the low-frequency region.

Figure 12. Charts. Example curve fitting of the representative spectrum of Na gel.

Fourier Transform Infrared Spectroscopy

The Fourier transform infrared spectroscopy (FTIR) analysis was carried out using a Fourier transform infrared spectrometer. The spectra of potassium bromide pellets with 0.3-percent sample concentration were collected at 4-cm^{-1} resolution and co-adding 32 scans per spectrum.

ICP Spectroscopy

The chemical compositions of the gels were verified using an ICP spectrometer. 0.5 g of each gel was mixed with 5.5 g of lithium tetraborate and 2 ml of a 0.5-g/L ammonium nitrate solution was fused at $980\text{ }^{\circ}\text{C}$. A total of three repetitions per gel were fused. The samples were digested using hydrochloric acid and then further diluted for the ICP analysis. The calibration of the ICP spectrometer was performed using corresponding Na^{2+} , K^{+} , Ca^{2+} , and Si standards. The coefficient of variation of the ICP analysis for each gel was less than 11 percent.

TGA

TGA was used to determine the amount of carbonation in and moisture content of the gels. The TGA was performed under nitrogen purge at 25 ml/min. Approximately 50 mg of powdered gel sample was heated to $950\text{ }^{\circ}\text{C}$ at $10\text{ }^{\circ}\text{C}/\text{min}$. The interpretation of the TGA curves was done following the procedure developed by Kim and Olek.⁽⁷⁵⁾

XRD

The diffractograms of the gels were collected with an XRD system. The x-ray source was a Cu anode operating at 45 kV and 40 mA. Data were collected between 10 to 80 degrees in 2θ with a step of 0.0131 degrees and scan step time of 99 s per step.

SEM-EDS

The SEM analysis was conducted using a microscope in secondary mode equipped with a concentric backscatter detector and coupled with EDS. The microscope was operated at 15 kV and a 10-mm working distance. The errors in the EDS measurements, caused by the surface effects due to the absence of a flat, polished surface, were minimized by considering atomic ratios.^(76,77)

CHAPTER 4. RESULTS AND DISCUSSION

INTRODUCTION

The research team used Raman spectroscopy to thoroughly characterize the structure of several synthetic ASR gels of controlled composition. The results were validated using additional techniques, such as FTIR, XRD, and TGA. There were two broad bands in the Raman spectra, one in the 800–1,200 cm^{-1} range and another in the 400–700 cm^{-1} range, indicating the amorphous nature of the gel. Important information regarding the silicate polymerization was deduced from both of these frequency regions. For validation, the trends in silicate depolymerization were also compared with results from an NMR spectroscopy study on similar synthetic ASR gels.⁽⁴⁶⁾

Further, the research team examined samples of ASR gel produced within a cementitious matrix using Raman spectroscopy to evaluate the potential of using this technique as a research or diagnostic tool to analyze samples closer to ASR-affected concrete from the field. Preliminary results indicated that the gels produced in these accelerated ASR samples had characteristic spectral features with predominantly Q^2 silicate sites. Although the technique is powerful and can easily deduce valuable structural information about ASR gels, the fluorescence of the adjacent cementitious matrix poses certain limitations to its extensive application in concrete and mortar samples.

The current study also explored an alternative method, SERS, to combat fluorescence associated with cementitious materials. A suspension of Ag nanoparticles was synthesized, applied on cement paste samples, and observed for its ability to reduce fluorescence and enhance the intensity of the Raman signal. The results indicated that the application of SERS to paste samples resulted in the enhancement of peaks in Raman spectra with some amount of spectral interference in certain regions due to the bands from the suspension. This chapter presents those results as well as a detailed characterization of the suspension of Ag nanoparticles and the influence of its deposition on the Raman signal.

GENERAL CHARACTERIZATION OF SYNTHETIC ASR GELS

The three series of synthetic ASR gels—sodium silica gels, potassium silica gels, and sodium calcium silica gels—will be referred to as Na gels, K gels, and Na-Ca gels, respectively, throughout the rest of this report. Table 7 summarizes the theoretical Na/Si, K/Si, and Ca/Si ratios as well as the exact ratios as determined by ICP spectroscopy. The slight variations in the ratios when compared to the target values were attributed to varying concentrations of the silicic acid sol obtained after exchange from the column. Further, the carbonation of the gels and the moisture content of the gels at the end of the drying period were also monitored using TGA. These results are also included in table 7. It is evident that, as the alkali/Si ratio of the gels increased, their ability to retain moisture also increased. The SEM coupled with EDS was used to confirm the full distribution of alkalis in the resulting gels (see the appendix for resultant data). The EDS maps were collected at five random locations on every sample of gel.

Table 7. Chemical composition, carbonation and moisture content of the synthetic ASR gels.

Gel Type	Gel Code	Target M*/Si Molar Ratio (Measured)	Target Ca/Si Molar Ratio (Measured)	Carbonation** (% by Weight)	Moisture Content (% by Weight)
Na	NS1	0.25 (0.21)	0.00	5.89	10.28
	NS2	0.50 (0.40)	0.00	3.01	13.06
	NS3	0.75 (0.62)	0.00	2.55	23.66
	NS4	1.00 (1.17)	0.00	4.21	20.87
K	KS1	0.25 (0.32)	0.00	2.23	8.63
	KS2	0.50 (0.58)	0.00	1.89	11.79
	KS3	0.75 (0.80)	0.00	3.82	12.52
	KS4	1.00 (1.08)	0.00	5.62	13.36
Na-Ca	NCS1	0.50 (0.37)	0.05 (0.07)	3.42	20.97
	NCS2	0.50 (0.35)	0.10 (0.11)	3.66	20.24
	NCS3	0.50 (0.37)	0.20 (0.25)	1.14	20.41
	NCS4	0.50 (0.36)	0.40 (0.49)	2.04	19.00

*M = Na or K.

**Carbonation percentage is qualitative and used merely to confirm presence of carbonates.

NS = Na gel series; KS = K gel series; NCS = Na-Ca gel series.

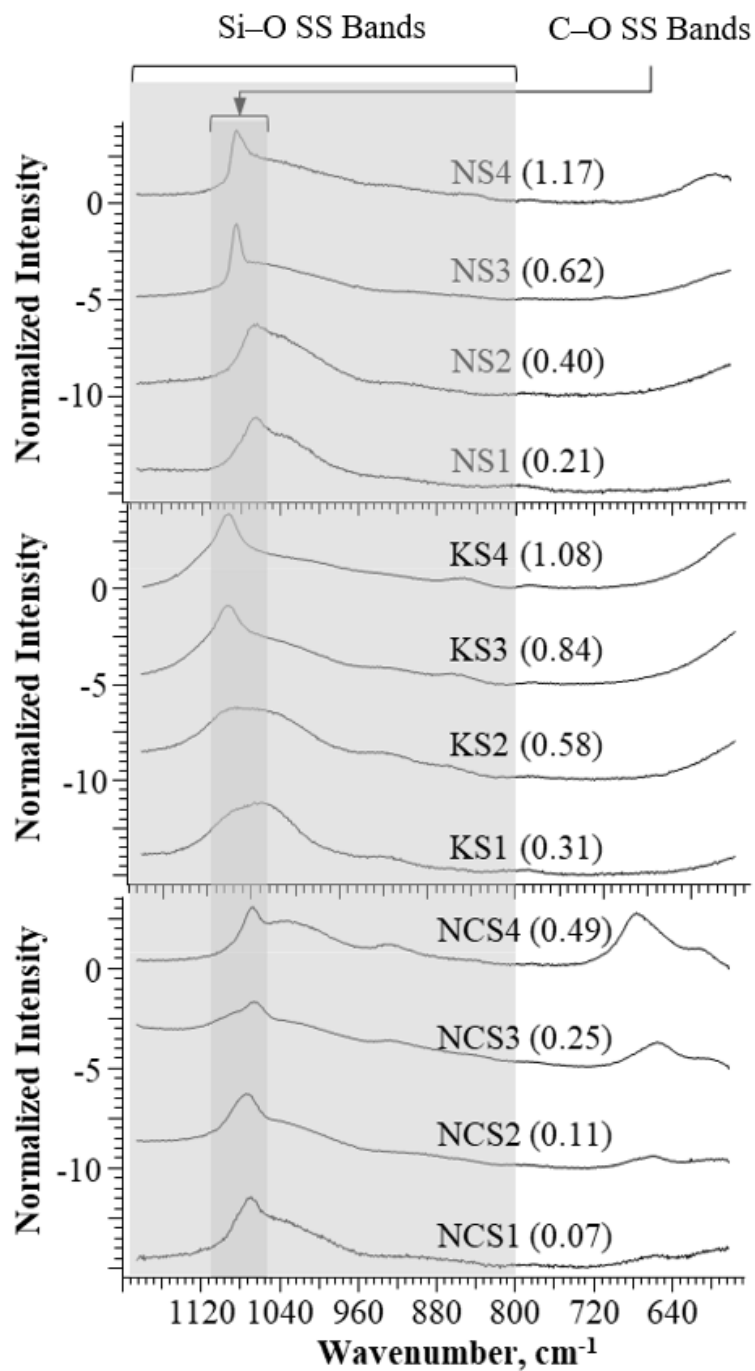
NORMAL DISPERSIVE RAMAN SPECTROSCOPY OF SYNTHETIC ASR GELS

Raman Spectroscopy of Synthetic ASR Gels

The broad peaks characterizing the Raman spectra of the Na, K, and Na-Ca gels, shown in figure 13, suggested the amorphous nature of the gels. Each spectrum had broad bands in mainly two regions of interest: the high-frequency region of 800–1,200 cm^{-1} and the low-frequency region of 400–700 cm^{-1} . The broad envelope in the high-frequency region contained peaks attributed to the Si–O SS bands of Q^0 (850 cm^{-1}), Q^1 (900 cm^{-1}), Q^2 (950–1,000 cm^{-1}), and Q^3 (1,050–1,100 cm^{-1}) silicate sites as well as the SS bands of the C–O bonds in carbonate phases. (See references 6, 34, 40, 41, and 78.) Bands in the low-frequency region were linked to the presence of bridging oxygens or Si–O–Si linkages and known to vary systematically with changes in composition, which in turn implied changes in the silicate polymerization.⁽⁶⁾ More specifically, bands in the 520–560 cm^{-1} range were linked to Q^3 silicate sites, 590–600 cm^{-1} range to Q^2 silicate sites, $\approx 700 \text{ cm}^{-1}$ to Q^1 silicate sites, and $\approx 430 \text{ cm}^{-1}$ to Q^4 silicate sites.⁽⁶⁾

Following the curve-fitting procedure discussed in the Raman Spectroscopy section in chapter 3, the spectra were then interpreted following an empirical approach that involved comparing the spectra with those from published literature for mainly amorphous materials, such as silicate glasses and C-S-H, as well as carbonate phases. (See references 6, 34, 40, 41, and 79–82). Table 8 through table 10 summarize the major bands that were deduced using curve fitting of the two broad bands in the low- and high-frequency regions for Na, K, and Na-Ca gels, respectively.

All the spectra had peaks in the 1,065–1080 cm^{-1} range due to the presence of one or more carbonate phases. XRD analysis confirmed the presence of these carbonate phases, and the extent of carbonation in each of the samples was quantified using TGA and is shown in table 7. The specific band assignments and trends in the Raman data are discussed separately for each of the frequency regions of interest in the following sections.

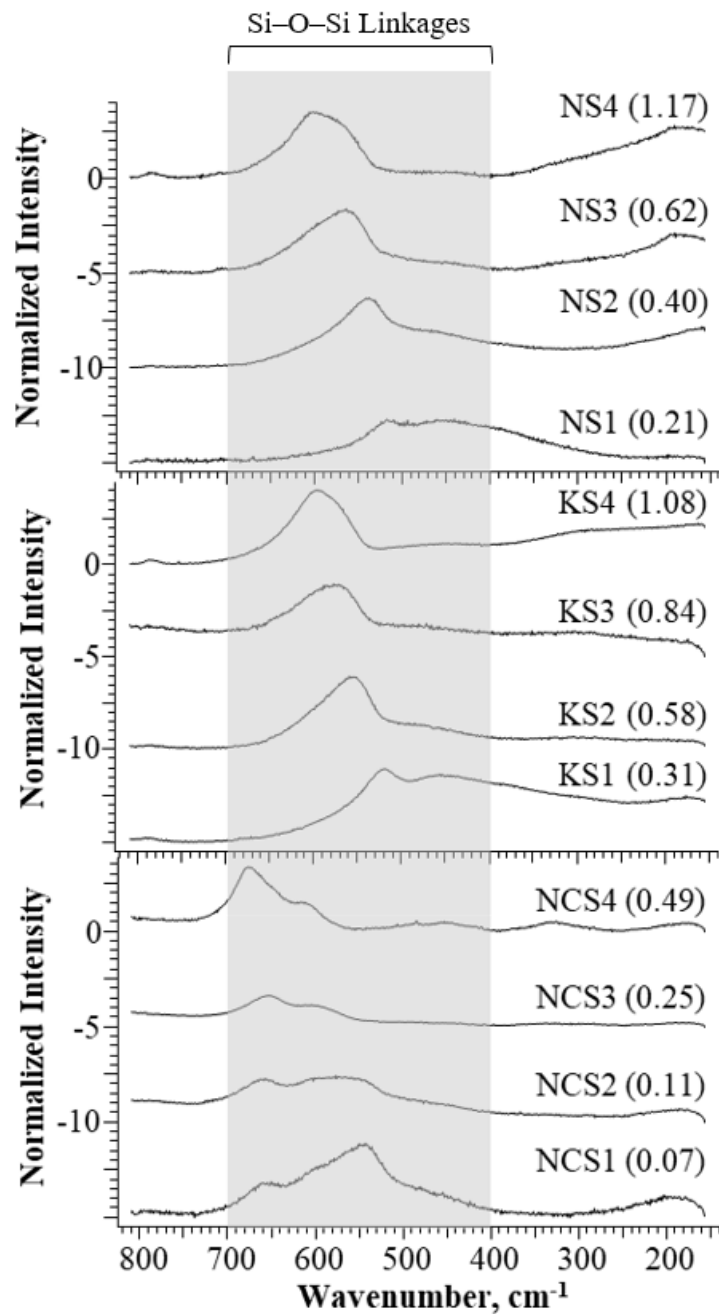


Source: FHWA.

NS = Na gel series; KS = K gel series; NCS = Na-Ca gel series.

Note: Gel codes and Na/Si, K/Si, or Ca/Si ratios are in parentheses. All Na-Ca gels have a fixed Na/Si ≈ 0.36 . All spectra are background subtracted.

A. Raman spectra for Na, K, and Na-Ca gels in the high-frequency region.



Source: FHWA.

NS = Na gel series; KS = K gel series; NCS = Na-Ca gel series.

Note: Gel codes and Na/Si, K/Si, or Ca/Si ratios are in parentheses. All Na-Ca gels have a fixed Na/Si ≈ 0.36 . All spectra are background subtracted.

B. Raman spectra for Na, K, and Na-Ca gels in the low-frequency region.

Figure 13. Charts. Raman spectra for synthetic alkali silica gels.

Table 8. Positions (cm⁻¹) and assignments of the principal vibrational bands in Raman spectra of Na gels.
(See references 6, 70, 79–81, 83, and 84.)

Gel Code (Na ₂ O/SiO ₂)				Assignments
NS1 (0.21)	NS2 (0.40)	NS3 (0.62)	NS4 (1.17)	
444.9	446.1	442.1	443.2	Si–O–Si linkages related to presence of Q ⁴ silicate sites
475.7	483.5	504.9	502.5	Internal deformations of Si–O tetrahedra or vibrationally isolated four-membered rings of SiO ₄ tetrahedra
518.2*	538.4*	558.0	559.6	Si–O–Si linkages related to presence of Q ³ silicate sites
574.8	596.8	595.2*	600.0*	Si–O–Si linkages related to presence of Q ² silicate sites
797.9	784.2	784.5	782.0	Motions of Si against tetrahedral O with little associated oxygen movement
—	861.2	860.2	849.2	Si–O SS of Q ⁰ tetrahedra
919.7	921.9	924.8	920.9	Si–O SS of Q ¹ tetrahedra
990.3	996.9	1,002.2*	1,006.0*	Si–O SS of Q ² tetrahedra or Si–OH
1,035.1*	1,037.2*	1,038.0	1,040.0	Si–O SS of Q ³ tetrahedra
1,066.0	1,067.5	1,071.4	1,067.9	Si–O SS of Q ³ tetrahedra or C–O SS of CO ₃ ²⁻ group (trona)
1,084.9	—	1,084.5	1,083.7	C–O SS of CO ₃ ²⁻ group (natrite)

*Most intense peaks in the low- or high-frequency regions.

—No data.

NS = Na gel series.

Table 9. Positions (cm⁻¹) and assignments of the principal vibrational bands in Raman spectra of K gels.
(See references 6, 70, 79–81, 83, and 84.)

Gel Code (K ₂ O/SiO ₂)				Assignments
KS1 (0.30)	KS2 (0.58)	KS3 (0.84)	KS4 (1.08)	
455.7	451.0	434.4	450.2	Si–O–Si linkages related to presence of Q ⁴ silicate sites
497.4	495.7	494.2	493.4	Internal deformations of Si–O tetrahedra or vibrationally isolated four-membered rings of SiO ₄ tetrahedra
526.7*	553.3*	566.0	562.3	Si–O–Si linkages related to presence of Q ³ silicate sites
579.4	595.2	595.8*	597.2*	Si–O–Si linkages related to presence of Q ² silicate sites
792.6	784.8	781.9	784.6	Motions of Si against tetrahedral O with little associated oxygen movement
851.0	857.6	852.4	847.6	Si–O SS of Q ⁰ tetrahedra
928.7	917.2	917.0	920.6	Si–O SS of Q ¹ tetrahedra
998.0	997.6	1,005.5*	1,000.1*	Si–O SS of Q ² tetrahedra or Si–OH
1,028.6*	1,043.2*	1,040.1	1,040.5	Si–O SS of Q ³ tetrahedra or C–O SS of CO ₃ ²⁻ group (kalicinite)
1,062.5	1,067.2	1,062.3	1,061.2	Si–O SS of Q ³ tetrahedra or C–O SS of CO ₃ ²⁻ group (potassium carbonate)

*Most intense peaks in the low- or high-frequency regions.

KS = K gel series.

Table 10. Positions (cm⁻¹) and assignments of the principal vibrational bands in Raman spectra of Na-Ca gels.
(See references 6, 70, 79–81, 83, and 84.)

Gel Code (CaO/SiO ₂)				Assignments
NCS1 (0.05)	NCS2 (0.10)	NCS3 (0.20)	NCS4 (0.40)	
—	—	438.96	445.6	Si–O–Si linkages related to presence of Q ⁴ silicate sites
484.3	471.2	487.1	485.2	Internal deformations of Si–O tetrahedra or vibrationally isolated four-membered rings of SiO ₄ tetrahedra
545.5*	557.2*	—	—	Si–O–Si linkages related to presence of Q ³ silicate sites
593.8	604.7	602.0	614.0	Si–O–Si linkages related to presence of Q ² silicate sites
656.8	656.3	650.4*	648.3	Si–O–Si linkages related to presence of Q ² silicate sites C-S-H
—	—	673.9	674.6*	Si–O–Si linkages related to presence of Q ¹ silicate sites C-S-H
794.4	794.4	794.4	794.4	Motions of Si against tetrahedral O with very little associated oxygen movement
—	—	856.9	—	Si–O SS of Q ⁰ tetrahedra
899.1	903.5	921.0	929.0	Si–O SS of Q ¹ tetrahedra
985.8	991.4	1,001.0*	1,012.0*	Si–O SS of Q ² tetrahedra or Si–OH
1,046.7*	1,040.5*	1,038.9	1,043.8	Si–O SS of Q ³ tetrahedra
1,068.2	1,071.5	1,064.0	1,069.1	Si–O SS of Q ³ tetrahedra or C–O SS of CO ₃ ²⁻ group (trona)
1,081.2	—	1,081.7	—	C–O SS of CO ₃ ²⁻ group (natrite)
—	1,086.8	1,085.5	1,085.0	C–O SS of CO ₃ ²⁻ group (calcite)

*Most intense peaks in both low- or high-frequency regions.

—No data.

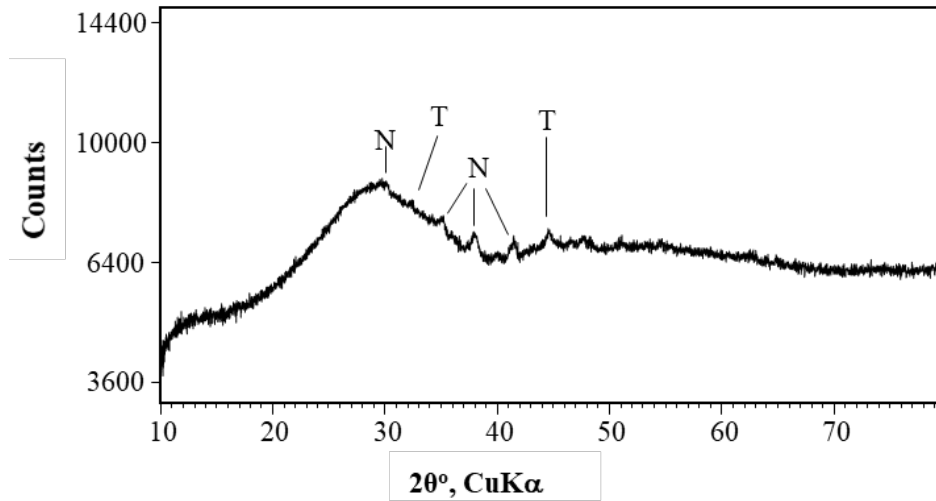
NCS = Na-Ca gel series.

High-Frequency Region (800–1,200 cm^{-1})

Based on the assignments in table 8 through table 10, the Raman spectra of the Na, K, and Na-Ca gels had peaks related to Si–O SS vibrations of Q^0 , Q^1 , Q^2 , and Q^3 silicate sites approximately near 855; 920; 1,000; and 1,040 cm^{-1} , respectively.

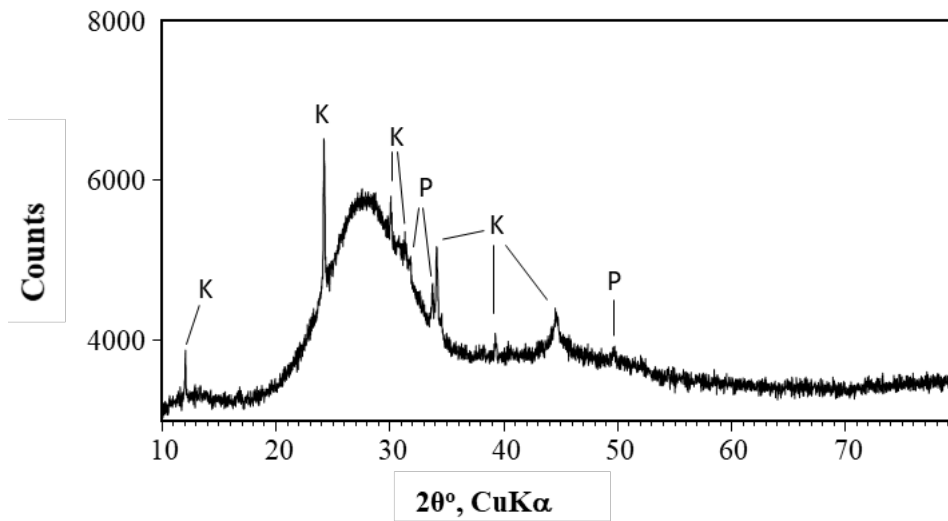
Before a detailed discussion of the results, it is important to point out possible areas where SS bands of the various silicate sites overlapped bands of other groups. There is a possibility that the bands of Q^2 silicate sites may have some contribution from a peak linked to the Si–OH stretching mode of silanol groups at $\approx 970 \text{ cm}^{-1}$.^(34,41,80) An attempt was made to confirm the stretching band of silanol in the synthetic gels at 950 cm^{-1} using FTIR.⁽⁸³⁾ However, this band of interest was obscured in the FTIR spectra by the broad band between 800 to 1,200 cm^{-1} attributed to the out-of-plane bending of carbonate groups, the Si–O–Si asymmetric stretching band, and vibrations of tetrahedral SiO_4 groups.^(84,85)

Another area of overlap was between the SS bands of Q^3 silicate sites and the C–O SS bands in carbonate groups, which appeared in the 1,030–1,090 cm^{-1} range for various Na, K, or Ca carbonate and bicarbonate phases. For some synthetic gels, the SS carbonate band appeared as a sharp peak, thus making their assignments straightforward. However, this was not always the case for others that overlapped the Si–O SS bands, resulting in a poorly resolved broad band. Most of the Na gel spectra had peaks around 1,065 and 1080 cm^{-1} , which were assigned to SS vibrational modes from the carbonate phases trona and natrite, respectively (table 8). The K gel spectra had peaks around 1,065 cm^{-1} attributed to SS vibrational modes in potassium carbonate (table 9). While not evident from the Raman data, there was also the possible existence of a peak around 1,030 cm^{-1} related to kalicinite. Similarly, the presence of trona, natrite, and calcite was observed in the Na-Ca gels as suggested by the presence of peaks at approximately 1,065; 1,080; and 1,086 cm^{-1} , respectively (table 10). Carbonation in the synthetic gel samples was confirmed using TGA (table 7) and XRD analysis. Figure 14 shows a representative x-ray diffractograms of each of the three different synthetic gel types with the phases linked to the major peaks. The XRD data supported the assignments made for the carbonate phases in the Raman data. Further, the presence of trona in ASR gel samples from the field has been noted in other published literature.⁽⁸⁶⁾



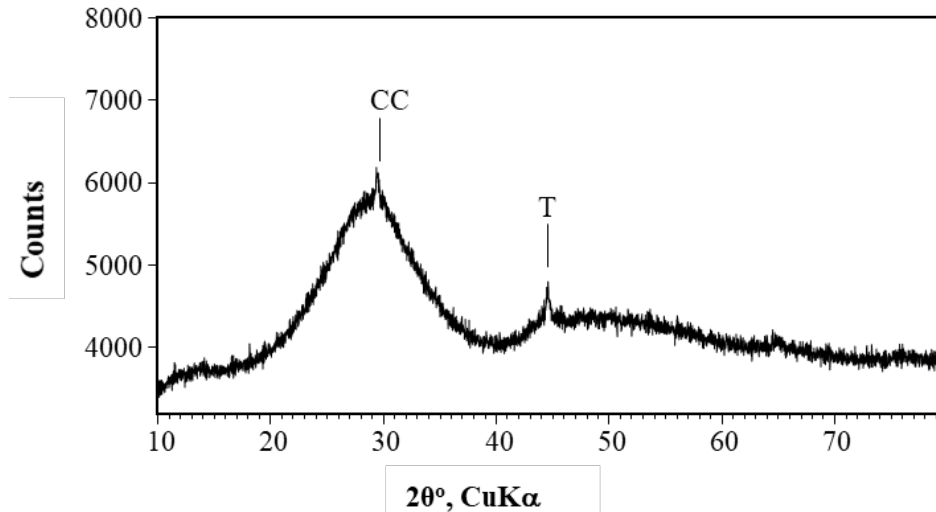
Source: FHWA.
 N = natrite; T = trona.

A. Principal diffraction peaks of carbonate phases in the x-ray diffractogram of synthetic Na gel (NS3).



Source: FHWA.
 K = kalicinite; P = potassium carbonate.

B. Principal diffraction peaks of carbonate phases in the x-ray diffractogram of synthetic K gel (KS2).



Source: FHWA.

CC = calcium carbonate; T = trona.

C. Principal diffraction peaks of carbonate phases in the x-ray diffractogram of synthetic Na-Ca gel (NCS2).

Figure 14. Charts. Principal diffraction peaks of carbonate phases in the x-ray diffractograms of synthetic alkali silica gels.

A close examination of table 8 through table 10 reveals that, for the Na and K gels, the most intense peak in the silicate SS region gradually shifted from $\approx 1,030$ to $\approx 1,000$ cm^{-1} with an increase in the alkali/Si ratio, suggesting a progressive depolymerization with increasing alkali content. However, the majority of the silicate sites in the gels with alkali/Si ratio less than 0.6 were Q^3 silicate sites. For the gels with an alkali/Si ratio between 0.6 and 1, Q^2 silicate sites were more prevalent. These gels with an alkali/Si ratio greater than 0.6 were beyond the normal range for ASR gels typically found in the field but were included to verify the fact that Raman spectroscopy can indeed detect changes in the polymerization of such systems. The observed shift in the SS band of the silicate sites with changing alkali/Si ratios has been reported in published literature and attributed to decreasing polymerization.^(6,41)

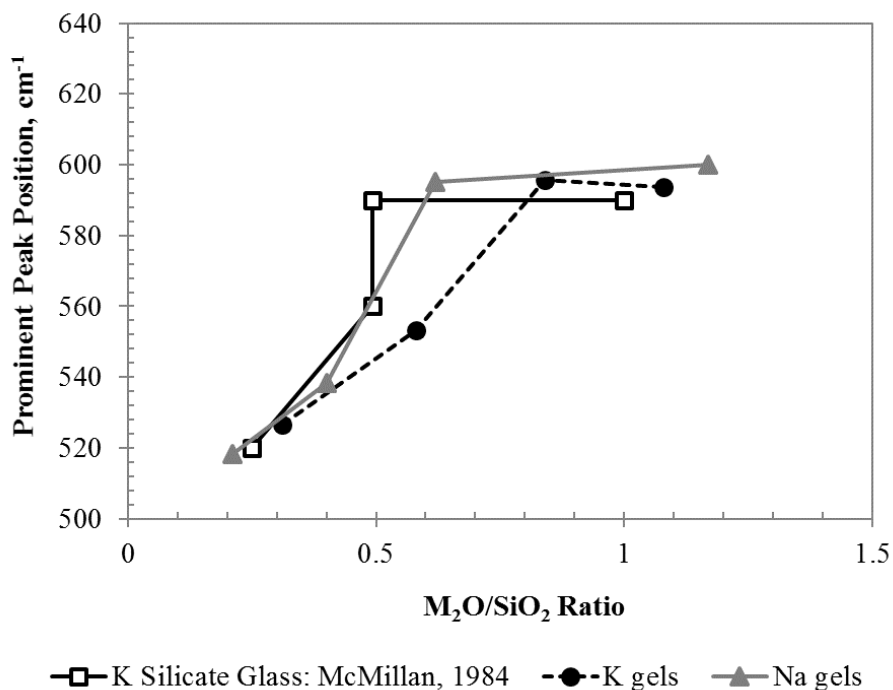
The Raman spectra of the Na-Ca gels displayed a similar shift in the most intense peak in the silicate SS region from 1,046 to 1,012 cm^{-1} , thus implying a progressive depolymerization with an increasing Ca/Si ratio, as observed in the Na and K gels. More specifically, the gels with a Ca/Si ratio less than 0.1 had more Q^3 silicate sites, while those with a ratio between 0.1 and 0.4 had more Q^2 silicate sites. The trends in the Na-Ca gels were more complex due to the fact that these gels may have contained two phases—an Na gel with calcium incorporated into the framework and C-S-H.⁽⁴⁶⁾ Thus, it may not be appropriate to extrapolate the trends in the Raman bands to the overall polymerization of the gels.

Low-Frequency Region (400–700 cm^{-1})

The low-frequency region of the Raman spectra of Na and K gels had bands linked to Si–O–Si linkages related to Q^4 , Q^3 , and Q^2 silicate sites at approximately 445, 520–560, and 595 cm^{-1} , respectively. For the Na-Ca gels, the Raman data analysis revealed bands of Q^4 , Q^3 , and Q^1

silicate sites at 440, 560, and 675 cm^{-1} , respectively. The assignment of the peaks related to Q^2 silicate sites was slightly more complex due to the fact that the curve-fitting procedure revealed the presence of two peaks—one at $\approx 600 \text{ cm}^{-1}$ and the other at $\approx 650 \text{ cm}^{-1}$ —in the spectral range valid for Q^2 silicate sites. The peak at $\approx 600 \text{ cm}^{-1}$ was assigned to Si–O–Si linkages related to the presence of Q^2 silicate sites in the Na silica gel with Ca incorporated into the framework, while the peak at $\approx 650 \text{ cm}^{-1}$ was assigned to similar Si–O–Si linkages in Q^2 silicate sites that are in the C-S-H phase (indicated as $\text{Q}^{2'}$ in figures). (See references 6, 34, 40, and 41.) The presence of the C-S-H phase in conjunction with Na-Ca silica gel has been previously reported for a similar system of Na-Ca silica gels with an Na/Si atomic ratio of 0.5 and Ca/Si atomic ratio greater than 0.23.⁽⁴⁶⁾ The presence of Q^2 peaks from both of these phases in the low-frequency region further corroborated this fact.

A close scrutiny of table 8 through table 10 indicates that the most intense peak in the low-frequency region for both Na and K gels shifted from ≈ 520 to $\approx 600 \text{ cm}^{-1}$. Figure 15 illustrates the change in position of the most intense peak in the Raman data of the Na and K gels used in this study with varying alkali/silica ratios and relevant data for alkali silicate glasses from published literature.⁽⁶⁾ Essentially, the phenomenon of decreasing silicate polymerization with increasing alkali content was prevalent both in the synthetic gels in this study as well as alkali silicate glasses. Table 8 through table 10 suggest that gels with an alkali/silica ratio less than 0.6 were mostly made of Q^3 silicate sites, while Q^2 silicate sites were predominant in those with alkali/silica ratios between 0.6 and 0.8. For the Na-Ca gels, peaks related to Q^3 silicate sites were prominent when the Ca/Si ratio was less than 0.1, while Q^2 silicate sites were more prevalent at a Ca/Si ratio of 0.2, and Q^1 silicate sites dominated the structure when the ratio is 0.4. As mentioned earlier in the discussion on the Raman spectral interpretations in the High-Frequency Region section, the trends reported for Na-Ca gels only reflect an overall polymerization of the gel and not necessarily changes in polymerization of the Na-Ca gel phase alone due to the possible presence of a C-S-H phase in conjunction with an Na-Ca gel.



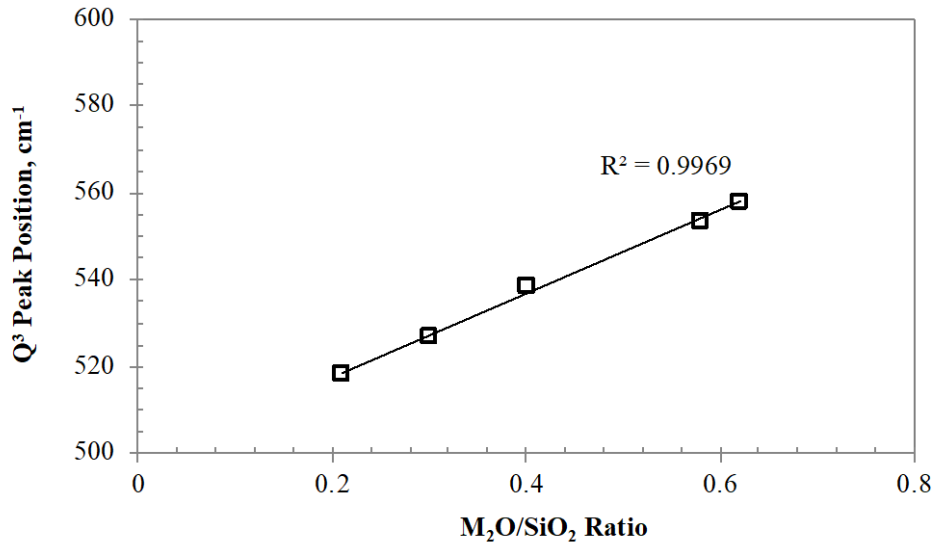
Source: FHWA.

M₂O = alkali oxide, where M is Na or K.

Note: Bands in 520-560 cm⁻¹ range are linked to Q³ silicate sites and 590-600 cm⁻¹ range to Q² silicate sites.

Figure 15. Graph. Relationship between the position of the most prominent peak in the Raman spectra (low-frequency region) and the alkali/silica ratio for Na and K gels and for K silicate glasses.⁽⁶⁾

As is evident in figure 15 and previously observed by McMillan et al., the peak linked to Q³ silicate sites displayed a progressive shift toward higher frequencies with increasing alkali content while the peak attributed to Q² silicate sites remained more or less stationary.⁽⁶⁾ The data of the position of the Q³ band only for gels with an alkali/silica ratio close to what can be expected in the field are replotted in figure 16. The strong correlation between the peak position of the Q³ (520–560 cm⁻¹) band in the Raman spectra of ASR gels and the alkali/silica ratio implied that these data could possibly be used to estimate the alkali/Si ratio of the gel. Thus, Raman spectroscopy could potentially be used as an easy tool to discern the chemical composition of the ASR gel without having to remove a sample and conduct a more detailed SEM-EDS investigation.



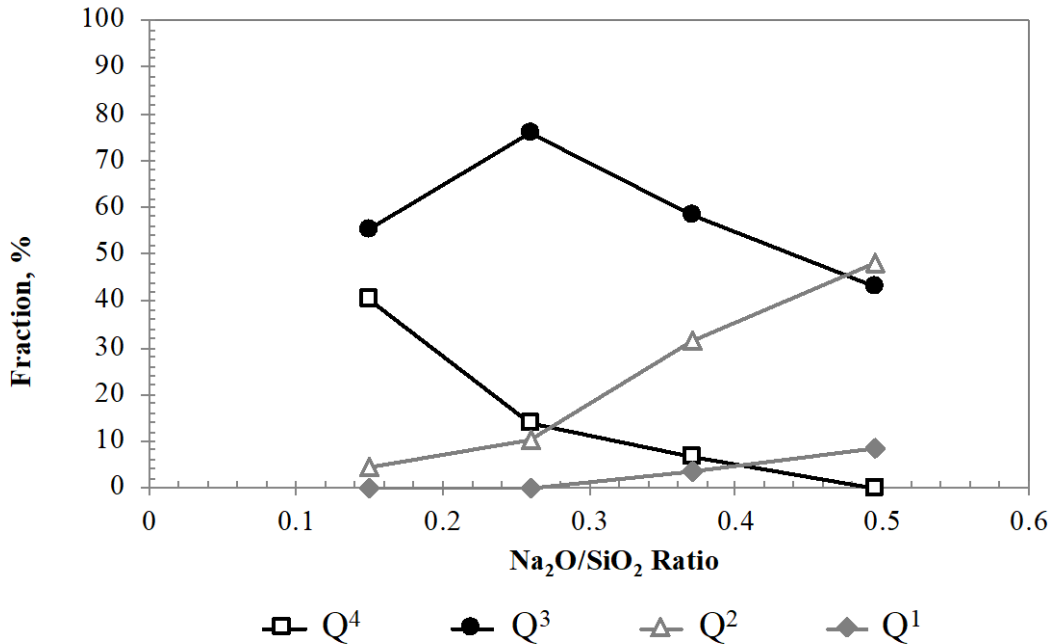
Source: FHWA.

M₂O = alkali oxide, where M is Na or K.

Figure 16. Graph. Relationship between the position of the peak linked to Q³ silicate sites and the alkali/silica ratio for Na and K gels.

Comparison of Raman Spectroscopic Data to NMR data

The polymerization information of the various synthetic gels was determined by analyzing the Raman spectra using the curve-fitting procedure and subsequent band assignments. This information was validated by comparing the results to a published ²⁹Si magic-angle spinning (MAS) NMR spectroscopy report on a series of synthetic alkali silica gels similar to the ones used in this current study.⁽⁴⁶⁾ Hou et al. reported that the gels had predominantly Q³ polymerization along with contributions to Q¹, Q², and Q⁴ silicate sites.⁽⁴⁶⁾ Figure 17 illustrates the fraction (percentage) of the various silicate polymerization sites present in the Na gels in this study, as determined from ²⁹Si MAS NMR data. In general, the ²⁹Si MAS NMR spectroscopy data revealed a progressive depolymerization in the synthetic alkali silica gels with increasing alkali content.

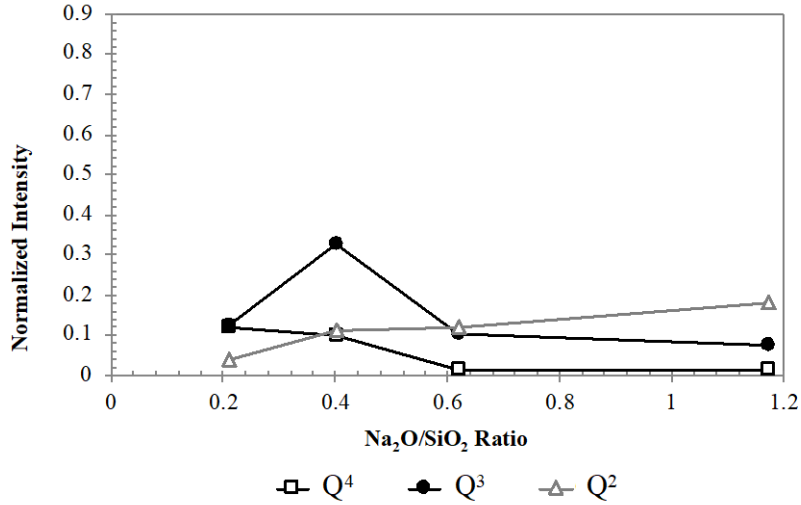


Source: FHWA.

Figure 17. Graph. Relationship between the fraction (percentage) of Q¹, Q², Q³, and Q⁴ silicate sites determined by the ²⁹Si MAS NMR and alkali/silica ratio for Na gels.⁽⁴⁶⁾

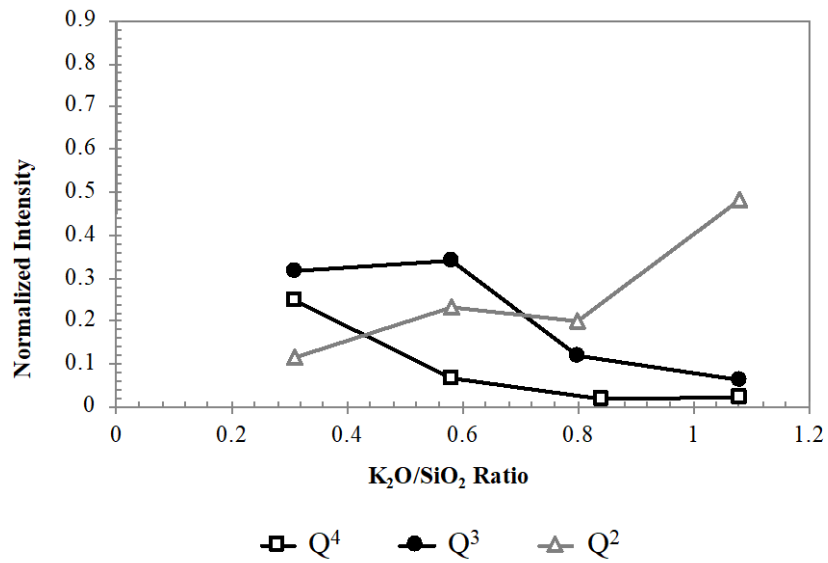
Figure 18 depicts the trends in the relative intensity of the peaks in the low-frequency region linked to Q¹, Q², Q³, and Q⁴ silicate sites in the Raman spectra for the Na, K, and Na-Ca gels. The assignments of certain bands in the high-frequency region were largely affected by the close proximity and possible overlapping of the C–O SS bands in carbonate groups as well as the peaks related to silanol groups, thus rendering a certain ambiguity to the trends described earlier in the High-Frequency Region section. Considering this fact, the data from the low-frequency region were chosen to draw more definitive conclusions regarding the polymerization of the gels with change in composition.

Figure 18 shows that, in the case of both the Na and K gels, there was an overall decrease in the relative intensity of the Q³ and Q⁴ peaks with increasing alkali/silica ratio, while that of the Q¹ and Q² peaks appeared to be increasing. The trends for Na-Ca gels were more complex due to the possible presence of two phases in the gel framework. The peaks related to Q³ silicate sites were observed only in the Na-Ca gels with a Ca/Si ratio of less than 0.1. The two types of Q² silicate sites, previously described in the Low-Frequency Region section, were found in all the Na-Ca gels with maximum relative intensity at a Ca/Si ratio of 0.2. The relative intensity of the peak associated with Q¹ silicate sites, found in the spectra of gels with a Ca/Si ratio of greater than 0.2, was found to increase with an increasing Ca/Si ratio. The presence of Q² and Q¹ silicate sites in the Na-Ca gels with a Ca/Si ratio of greater than 0.2 further substantiated the possible coexistence of a C-S-H phase as well as an Na-Ca silica gel since these sites were more predominant in C-S-H than Q³ silicate sites.^(41,87,88)



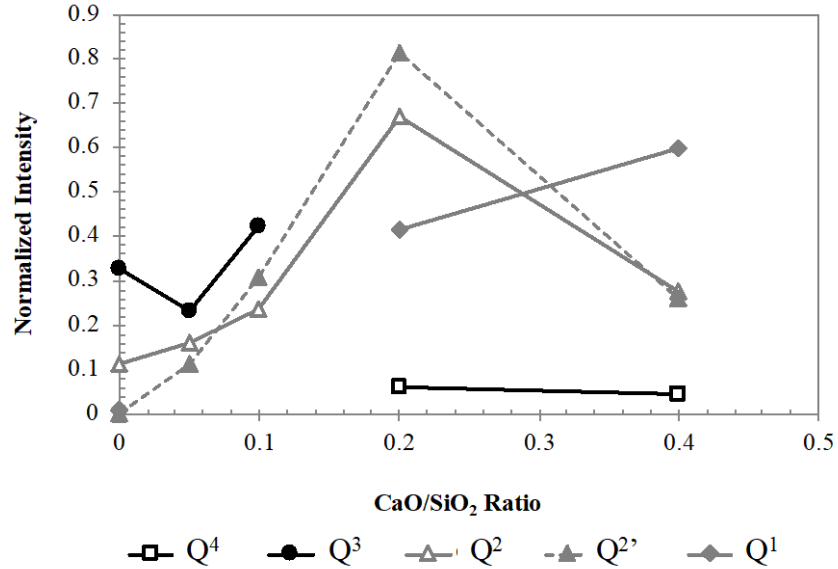
Source: FHWA.

A. Relationship between the normalized intensity of the Q², Q³, and Q⁴ peaks in the low-frequency region and Na₂O/SiO₂ ratio in Na gels.



Source: FHWA.

B. Relationship between the normalized intensity of the Q², Q³, and Q⁴ peaks in the low-frequency region and K₂O/SiO₂ ratio in Ka gels.



Source: FHWA.

C. Relationship between the normalized intensity of the Q¹, Q², Q³, and Q⁴ peaks in the low-frequency region and CaO/SiO₂ ratio in Na-Ca gels.

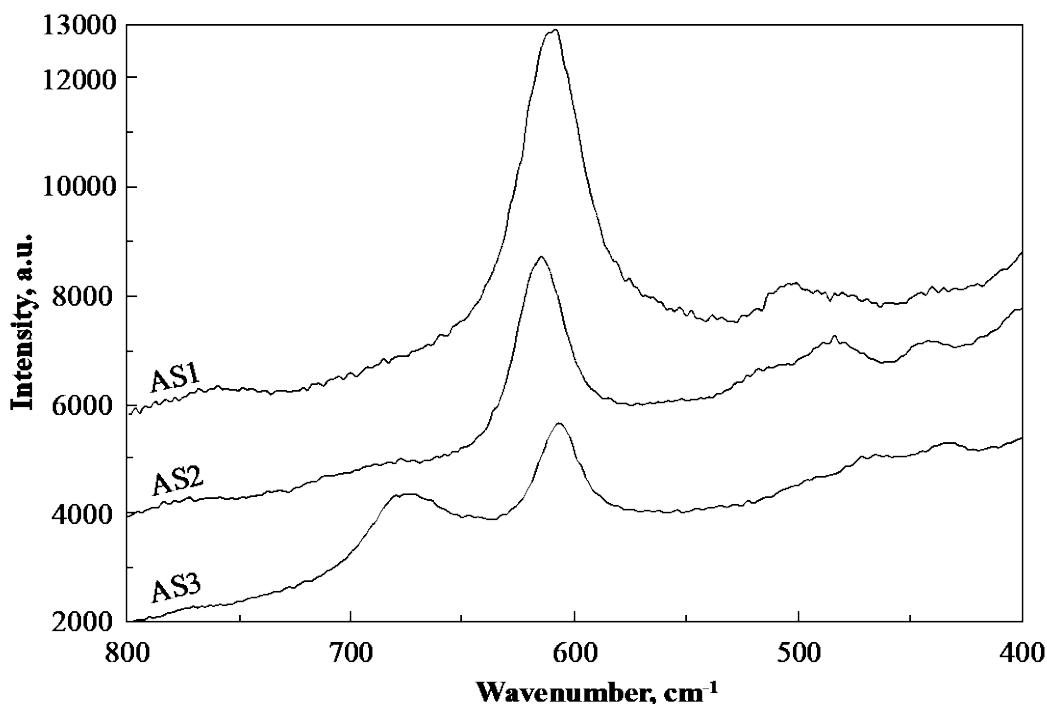
Figure 18. Charts. Relationship between the normalized intensity of Q¹, Q², Q³, and Q⁴ peaks in the low-frequency region and the alkali/silica or Ca/Si ratio in synthetic alkali silica gels.

In general, the trends in the fraction (percentage) of the Q¹, Q², Q³, and Q⁴ silicate sites in the gels, as reported by NMR and shown in figure 17, were in agreement with the low-frequency region Raman data presented in figure 18. Based on the NMR data, Hou et al. reported that all the gels with a Na/Si ratio of less than 0.495 comprised predominantly Q³ sites, while the gels with a ratio of 0.495 had slightly more Q² silicate sites. As evident in figure 15, gels with a Na/Si ratio of less than 0.62 were dominated by Q³ silicate sites, while the gels with higher Na/Si ratios had more Q² silicate sites. Further, as emphasized in the Low-Frequency Region section, the presence of a C-S-H phase in conjunction with the Na-Ca gel phase, especially in the gels with a Ca/Si ratio of greater than 0.2 reflected similar observations by Hou et al. based on XRD and NMR data.⁽⁴⁶⁾ In general, the Raman data presented in this report mirrored the trend of depolymerization with increasing alkali/silica ratios, which has been previously reported using ²⁹Si MAS NMR spectroscopy.⁽⁴⁶⁾

NORMAL DISPERSIVE RAMAN SPECTROSCOPY OF ASR SAMPLES AND CEMENT PASTE

The Raman spectra collected from the accelerated samples (AS1, AS2, and AS3) are discussed briefly in this section. As described in the Accelerated ASR Sample section in chapter 3, the purpose of this part of the study was not to obtain a thorough Raman characterization of the ASR gels but to evaluate the potential of applying this technique to field samples. As a result, only a broad structural interpretation of the most prominent bands is provided for the spectra.

In general, the Raman spectra collected from ASR gels in all three samples were reasonably resolved, containing a number of distinct bands despite considerable background fluorescence in most cases. Structural interpretations of the bands were based on band assignments in published literature for mainly amorphous materials, such as silicate glasses and C-S-H as well as carbonate phases. (See references 6, 34, 40, 41, and 79–82.)



Source: FHWA.
a.u. = arbitrary units.

Figure 19. Chart. Low-frequency region of Raman spectra of gels from accelerated ASR samples.

Table 11. Positions (cm^{-1}) and assignments of the principal vibrational bands in the low-frequency region of Raman spectra of gels from accelerated ASR samples.^(6,80,81)

AS1	AS2	AS3	Assignments
—	443	—	Si–O–Si linkages related to presence of Q^4 silicate sites
500	484	—	Internal deformations of Si–O tetrahedra or vibrationally isolated 4-membered rings of SiO_4 tetrahedra
—	515	—	Si–O–Si linkages related to presence of Q^3 silicate sites
610	615	607	Si–O–Si linkages related to presence of Q^2 silicate sites
—	—	674	Si–O–Si linkages related to presence of Q^1 silicate sites C-S-H

—No data.

Figure 19 shows the low-frequency region of the Raman spectra of samples AS1, AS2, and AS3. As elaborated in the Normal Dispersive Raman Spectroscopy of Synthetic ASR gels section, the high-frequency region of the Raman spectra of gels was possibly influenced by overlapping of the C–O SS bands in carbonate groups and peaks related to the silanol group. Consequently, only the low-frequency region, shown in figure 19, was used for a broad structural assignment. A

detailed analysis including spectral processing and curve fitting for this set of samples was beyond the scope of the current study. The structural assignments provided in table 11 are based on the most dominant peaks and do not cover the bands that could not be deduced without processing the spectra using a curve-fitting procedure.

Based on the Raman data of sample types AS1, AS2, and AS3, the ASR gel produced was dominated by silicate tetrahedral of Q^2 polymerization. Raman spectra of gels from AS2 and AS3 revealed traces of Q^3 and Q^1 silicate sites from C-S-H respectively. As discussed in the Low-Frequency Region section, synthetic ASR gels with alkali/silica molar ratios greater than 0.6 had predominantly more Q^2 silicate sites. Such values of alkali/silica molar ratios are rather unusually high for field samples. However, considering the fact that the gels in AS1, AS2, and AS3 were produced by aggressive exposure conditions to 1N NaOH, it is possible that the elevated alkalinity in the pore solutions in the samples promoted the formation of an ASR gel with alkali content higher than what would be expected in the field. Again, structural interpretations described here are quite primitive due to the fact that there may be bands obscured by a combination of high background fluorescence and overlapping bands.

POSSIBLE CHALLENGES IN USING RAMAN SPECTROSCOPY AS A DIAGNOSTIC TECHNIQUE

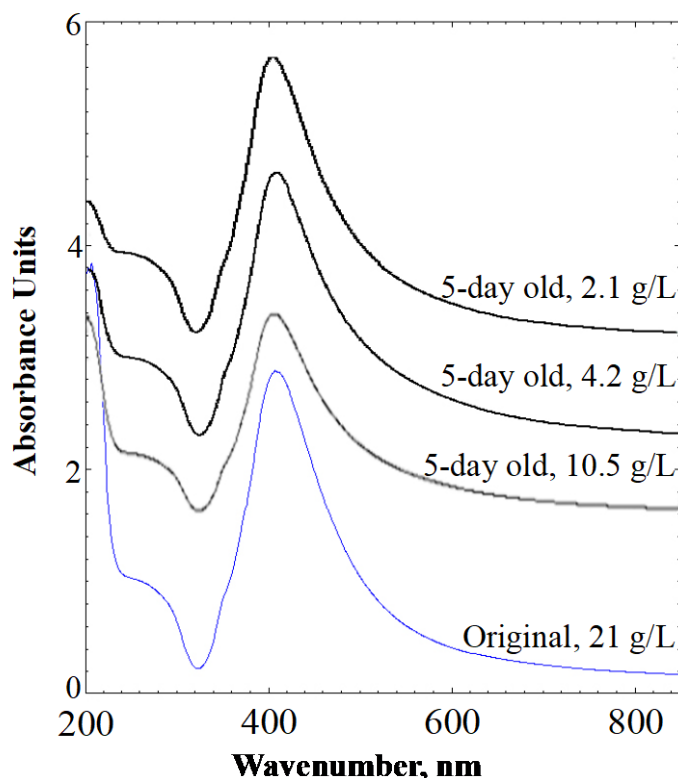
Raman spectroscopy is unquestionably a powerful tool to explore the local structure of an ASR gel. However, there are some issues that should be considered while looking into the possible development of this technique as a diagnostic tool in the field:

- On several occasions, the in-situ analysis of ASR gels within the mortar or concrete specimen proved to be challenging on account of fluorescence of adjacent cementitious phases. Raman spectra of good quality were successfully collected from ASR gel deposits within voids larger than 100 μm . However, obtaining Raman spectra of reasonable quality from smaller deposits or gel lining cracks was often challenging. Considering this fact, the use of this technique in early stages of ASR distress may not be practical.
- While the excitation volume of the laser beam can be made quite small (approximately a couple cubic microns depending on excitation wavelength, magnification of lens, material, laser power, etc.), there may still be contribution of photons from other neighboring phases, such as C-S-H, which can further complicate diagnosis.
- In many cases, cracking due to ASR may be observed, to a large extent, with scarce deposition of gel. In these cases, the lack of sizeable amounts of gel may preclude the use of this technique. In other words, there may be field conditions that require the technique to be highly sensitive. However, in the event that visible deposits of the ASR gel are present, there is still no accurate technique to identify it in situ. Thus, developing a Raman diagnostic technique may still be a worthwhile effort.

SERS OF CEMENT PASTE

Characterization of Ag Nanoparticle Suspension

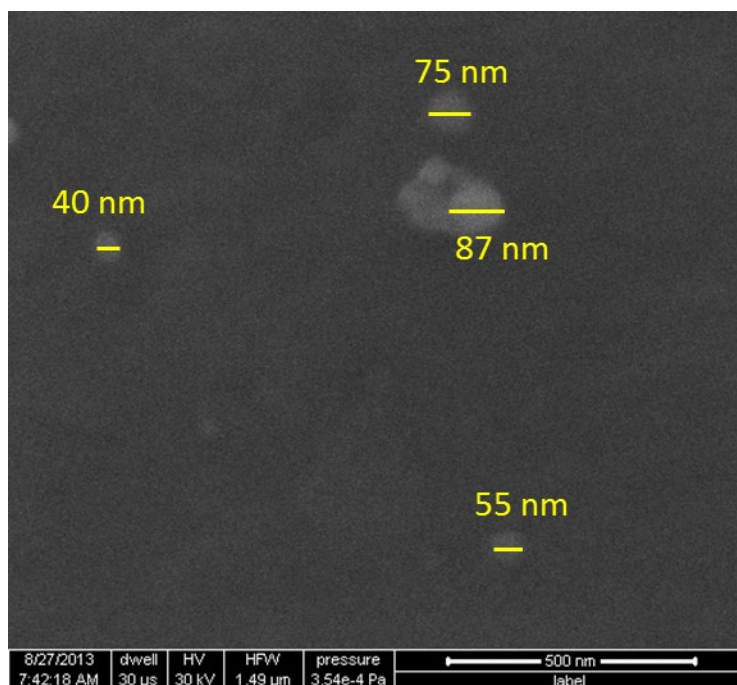
The quality of the Ag nanoparticle suspension produced, as described in the SERS Nanoparticle Suspension section, was validated by measuring the UV-Vis absorbance maximum. The absorbance maximum was 420 nm, which is in agreement with that mentioned in published literature.⁽⁶⁸⁾ The chemical stability of the suspension over time and with respect to concentration was evaluated by tracking the maximum absorbance value at 5 d at different dilution factors: 2, 5, and 10 times. The results are summarized in figure 20. The 420-nm value of the maximum absorbance remained constant despite the changes in suspension concentration.



Source: FHWA.

Figure 20. Chart. UV-Vis absorption spectra of Ag nanoparticle suspension with respect to time and suspension concentration.

The SEM characterization of a drop of suspension deposited on an aluminum surface revealed that the Ag nanoparticles were approximately 50 nm in diameter with agglomerates of up to 100 nm in diameter, as shown in figure 21. Raman measurements were taken on the Ag nanoparticle suspension to clearly identify the peaks that may appear in the SERS spectra of samples, which may be attributed to the suspension itself. The characteristic Raman bands of an Ag nanoparticle suspension with a 2.1-g/L concentration with the corresponding assignments are summarized in table 12.



Source: FHWA.

Figure 21. Micrograph. SEM micrograph of a Ag nanoparticles.

Table 12. Characteristic Raman bands and assignments of the Ag nanoparticle suspension.⁽⁹⁰⁾

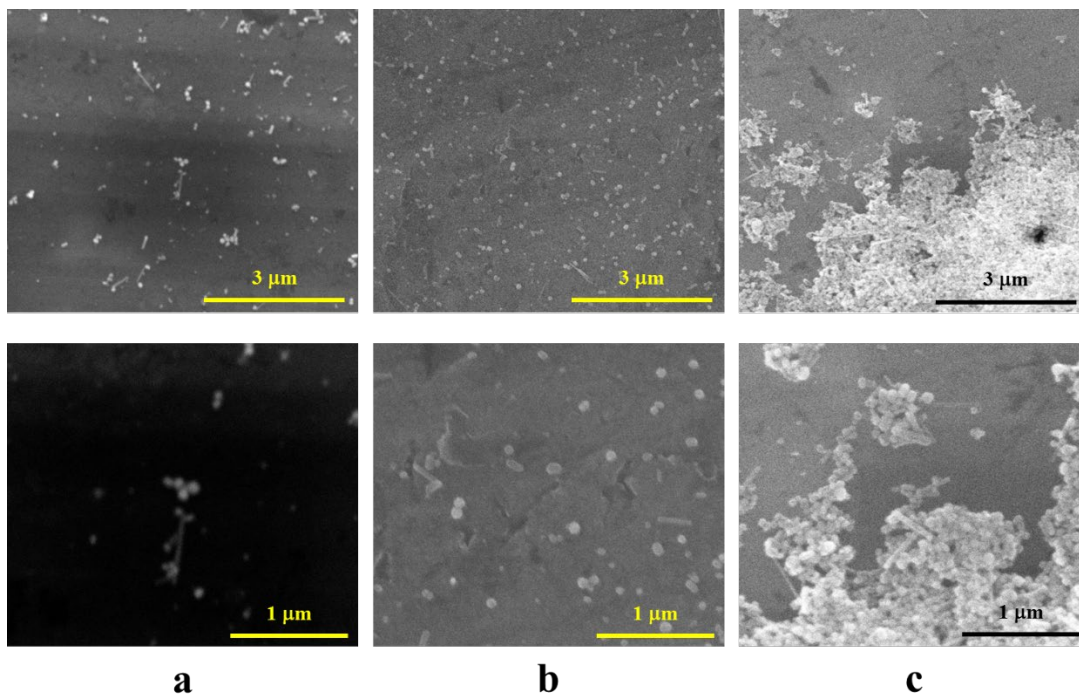
Band (cm ⁻¹)	Assignment
532	Rhodamine
617	Rhodamine
691	—
817	Citrate
937	Rhodamine
1,059	Citrate
1,330	Citrate

—No data.

Influence of Surface Deposition of Ag Nanoparticle Suspension in Raman Signal

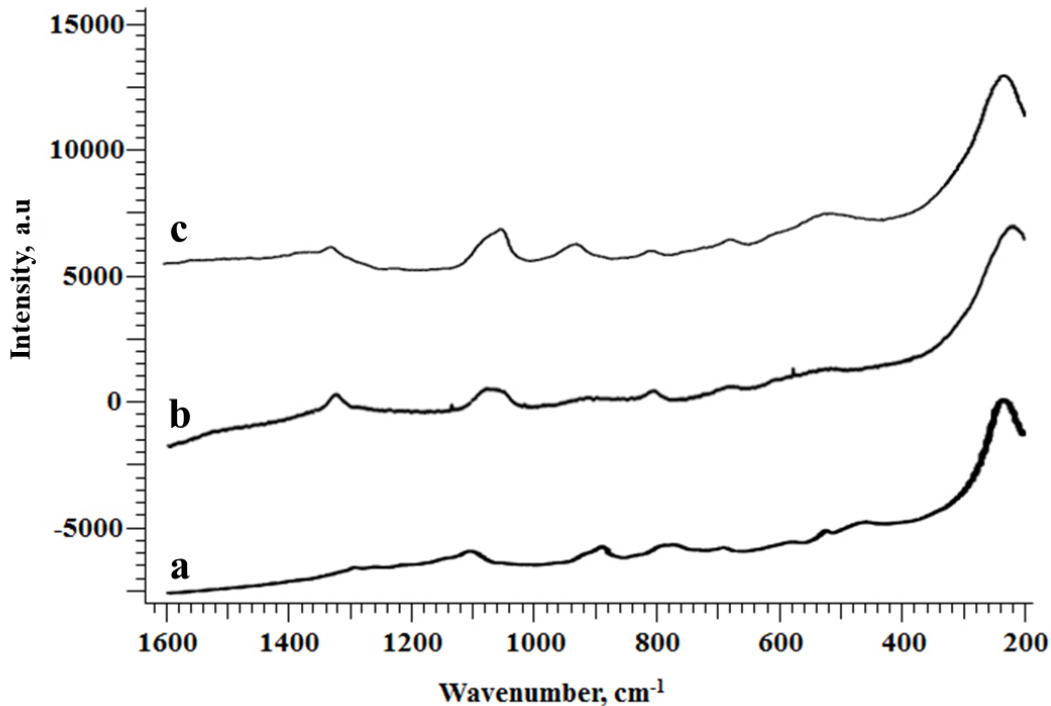
The main advantage of using SERS-activated nanospheres for enhanced Raman characterization of cementitious materials is the simplicity of the synthesis process and possibility to produce size-controlled nanoparticles. The SERS effect is highly dependent on the size, shape, and aggregation of the nanospheres. For this study, the nanospheres were obtained as suspension by the reduction of the metal salt with reducing and stabilizing agents. The SERS-active spots are normally localized in the interface between the metallic nanospheres. Normally, in this SERS active spot, aside from the sample of interest, reducing agents from the synthesis process can also be present. This fact, in conjunction with the limited control of aggregation when the suspensions are applied as films over solid samples, can lead to uncontrolled changes in the intensity of the SERS effect.⁽⁸⁹⁾

The following experiment was designed to study the aggregation effect in the SERS spectra. The Ag nanoparticle suspensions were applied over an aluminum surface using a dip-coating approach. The suspension concentration was the main variable of the experiment. SEM micrographs and Raman spectra were collected from the coated aluminum surfaces. The results are illustrated in figure 22. As the concentration of suspension increased, the level of aggregation of the Ag nanoparticles also increased, and the intensity of a group of bands in the spectra consistently increased. Table 12 lists the observed bands with relevant band assignments. Some of the bands were associated to citrate molecules, which were used as reducing agents during the synthesis and located on the surface of the nanoparticle.⁽⁹⁰⁾



Source: FHWA.

A. SEM micrographs of Ag nanoparticle deposits on an aluminum surface at different concentrations: (a) 0.42-g/L Ag nanoparticle suspension and 15 coatings; (b) 2.1-g/L Ag nanoparticle suspension and 2 coatings; and (c) 8.4-g/L Ag nanoparticle suspension and 2 coatings.



Source: FHWA.
a.u. = arbitrary units.

B. Raman spectra of Ag nanoparticles deposited on an aluminum surface at different concentrations: (a) 0.42-g/L Ag nanoparticle suspension and 15 coatings; (b) 2.1-g/L Ag nanoparticle suspension and 2 coatings; (c) 8.4-g/L Ag nanoparticle suspension and 2 coatings.

Figure 22. Micrographs and chart. Correlation between suspension deposition (SEM micrograph) and peaks in Raman spectrum of aluminum surface coated with varying concentrations of Ag nanoparticle suspension.

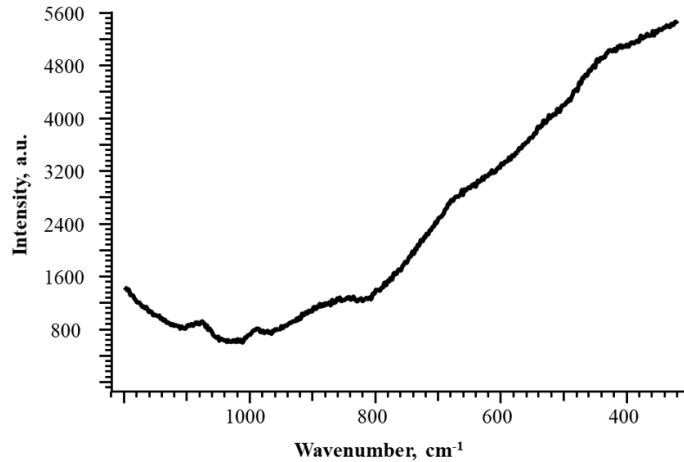
Application of SERS on Cementitious Materials

The results discussed in the Influence of Surface Deposition of Ag Nanoparticles Suspension in Raman Signal section clearly illustrate how the deposition of excess suspension during SERS application caused inherent peaks from the nanoparticles, further complicating identifying peaks from the sample. A set of experiments was conducted to investigate the possibility of applying SERS on alkali silica gels and OPC-paste samples, determine the nature of the peaks generated, and highlight the potential overlap of bands from the Ag nanoparticle suspension and frequency regions of interest for ASR gels, C-S-H, and other common OPC hydration products. The major observations from these experiments as well as selected examples are described in the following sections.

SERS Enhancement

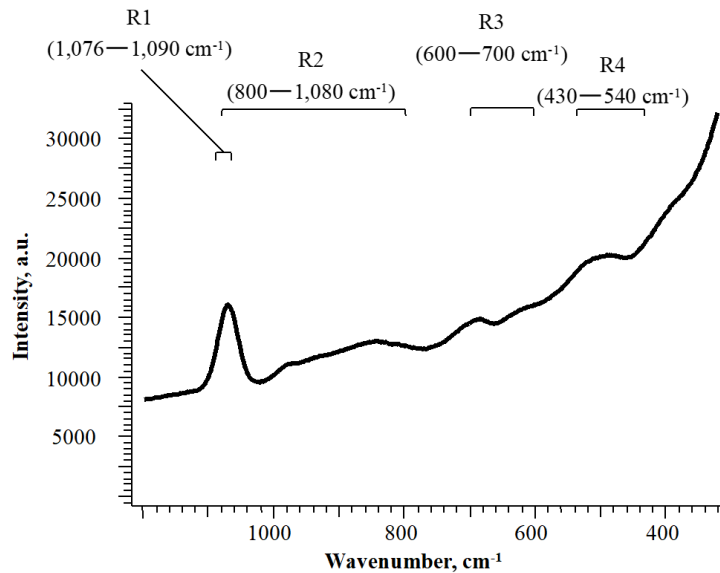
The most striking observation after collecting the SERS spectra of the various samples was that this technique did indeed appear to aid in combating the undesired fluorescence associated with the cementitious materials. Figure 23 shows the normal dispersive Raman spectrum as well as the SERS spectrum (figure 23-B) of a sample of OPC paste after 7 d of hydration. It is evident

from the SERS spectrum that the intensity of the Raman signal was greatly enhanced, thus allowing more visible spectral details over the broad fluorescent signal observed in the same region in the normal Raman spectrum. The regions R1, R2, R3, and R4 shown in figure 23-A are the major frequency regions of interest for cement paste with the corresponding assignments summarized in table 13. As is evident from figure 23-B, the new peaks in the SERS spectrum of the cement paste appear, to a large extent, in expected positions.



Source: FHWA.
a.u. = arbitrary units.

A. Dispersive Raman spectrum of OPC samples after 12 h of hydration before SERS application.



Source: FHWA.
a.u. = arbitrary units.

B. Dispersive Raman spectrum of OPC samples after 12 h of hydration after SERS application of a 16.8-g/L Ag nanoparticle suspension.

Figure 23. Charts. Dispersive Raman spectrum of hydrated OPC samples before and after SERS application.

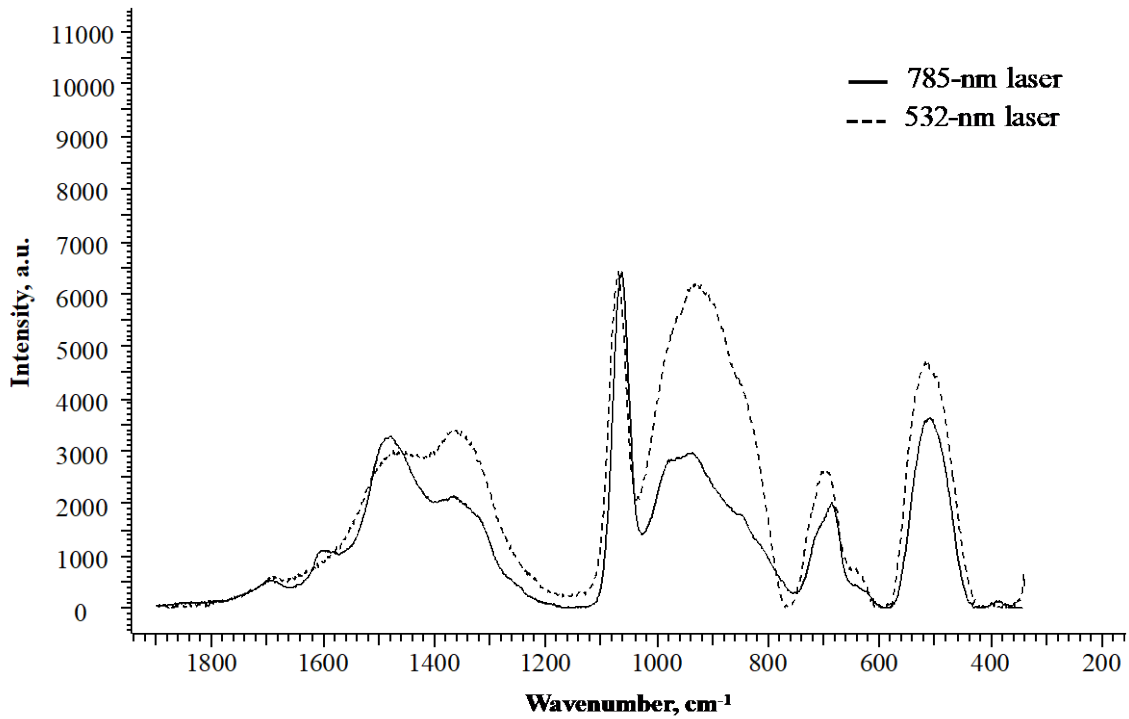
Table 13. Characteristic Raman regions of hydrated OPC sample.

Region (Wavenumber in cm^{-1})	Band Assignment
R1 (1,090–1,076)	$\nu_1 \text{CO}_3^{2-}$
R2 (1,080–800)	Symmetric stretching of SiO_4 tetrahedra or $\text{Si-O(H)}/\nu_1 \text{SO}_4^{2-}$
R3 (600–700)	Symmetrical bending of Si-O-Si linkages
R4 (430–540)	Internal deformations of Si-O tetrahedra

ν_1 = symmetric stretching.

Verification of Raman Peaks

The research team conducted a simple test was conducted to verify that the spectral bands produced when applying SERS were true Raman peaks. This test involved determining if the positions of the peaks in the spectrum remain independent of the excitation wavelength used to collect the spectrum.⁽¹⁹⁾ In this study, the spectra of various samples were collected at two different excitation wavelengths, 785 and 532 nm. As shown in figure 24, laser wavelength did not affect the position of the bands in all of the samples tested, thus ensuring that the peaks generated were entirely due to the Raman effect.



Source: FHWA.

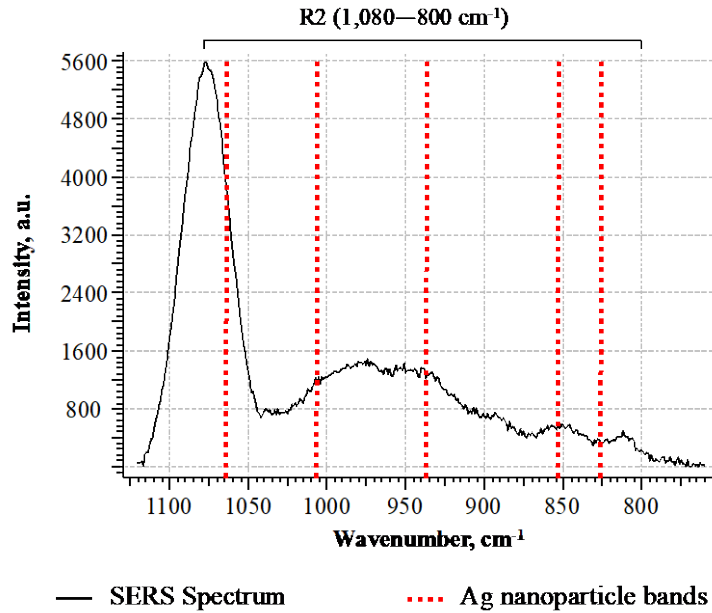
a.u. = arbitrary units.

Note: 16.8-g/L Ag nanoparticle suspension.

Figure 24. Chart. SERS spectra of OPC with 10% silica fume (water/cementitious-material ratio = 0.45) after 4 d of hydration collected using 785- and 532-nm lasers.

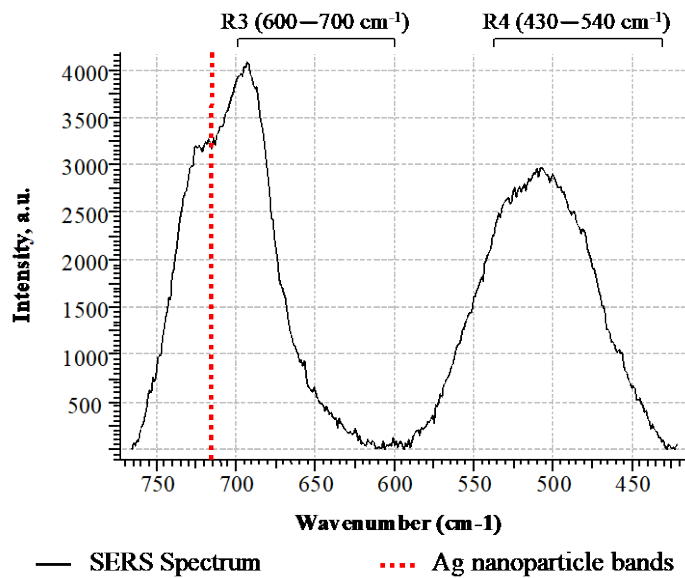
Spectral Interference of Ag Nanoparticle Suspension

While the SERS technique seems promising, it is essential that the SERS spectrum is interpreted with utmost care. The deposition of the Ag nanoparticles on the sample may cause some spectral interference and induce some shifts in the actual peaks of the sample. Figure 25 shows the specific portion of the nanoparticle spectrum that may interfere with the sample spectra. Displayed in figure 23-B and described in table 13 are the assignments for the frequency regions of interest where one might expect the vibrational bands of the cementitious systems to appear. Figure 25 shows high- and low-frequency regions of a SERS spectrum of a 7-day-old hydrated cement-paste sample collected using a 16.8-g/L Ag nanoparticle suspension. The grey shaded areas in the figure indicate expected frequency regions for peaks related to cement hydration, and the dotted lines indicate the peaks that appear as a result of aggregation of the Ag nanoparticles on the paste surface. It is evident from figure 25 that the Raman signal of the sample spectra in the carbonate stretching, silicate stretching, and silicate bending vibration regions (R1, R2, and R3, respectively) had potential contributions from the Ag nanoparticles. Nevertheless, the Ag nanoparticle peaks were quite sharp and well resolved, making them clearly distinguishable from the broader peaks in the silicate vibrational region of the sample spectra due to their amorphous nature, especially at later ages. As is further evident in figure 25, there were areas in the silicate stretching regions of $1,000\text{--}970\text{ cm}^{-1}$ and $920\text{--}830\text{ cm}^{-1}$ that were devoid of any contribution from the nanoparticles, and the Raman signal, if present in these areas, would have been easily visible in the SERS spectra of the samples.



Source: FHWA.
a.u. = arbitrary units.

A. Spectral interference from the Ag nanoparticles in SERS spectrum of 7-day-old hydrated cement paste (water/cement ratio = 0.45) collected with a 16.8-g/L Ag nanoparticle suspension in the high-frequency region.



Source: FHWA.
a.u. = arbitrary units.

B. Spectral interference from the Ag nanoparticles in SERS spectrum of 7-day-old hydrated cement paste (water/cement ratio = 0.45) collected with a 16.8-g/L Ag nanoparticle suspension in the low-frequency region.

Figure 25. Charts. Spectral interference from a Ag nanoparticles on 7-day-old hydrated cement paste.

CHAPTER 5. SUMMARY, CONCLUSIONS, AND RECOMMENDATIONS

SUMMARY

The research discussed in this report confirms the suitability of applying Raman spectroscopy to study ASR gels. The technique was used to deduce relevant structural information of ASR gel in synthetic systems as well as mortar and concrete samples.

A new analysis protocol was proposed based on the thorough characterization of synthetic ASR gels. The results were validated by published literature. Further, an attempt was made to use Raman spectroscopy to characterize ASR gels within concrete and mortar samples, and the limitations of applying this technique to probe products within a cementitious matrix were identified. The inherent fluorescence associated with these materials was identified as the main limitation that obscured important spectral information of the samples.

Finally, the potential benefits of developing a technique based on SERS for concrete materials to reduce fluorescence was discussed. Preliminary results showcasing the enhancement produced in the Raman peaks of cement-paste samples were presented, and the role of aggregating Ag nanoparticles in the Raman signal was discussed.

CONCLUSIONS AND RECOMMENDATIONS

Based on the results discussed within the report the research team identified the following conclusions and recommendations:

- The Raman spectra of synthetic ASR gels were characterized as having two broad bands in the 800–1,200 cm^{-1} (high-frequency) range and the 400–700 cm^{-1} (low-frequency) range, indicating the amorphous nature of the gel. The high-frequency range in the Raman spectra of all the synthetic gels had Si–O SS peaks of Q^0 (855 cm^{-1}), Q^1 (920 cm^{-1}), Q^2 (1,000 cm^{-1}), and Q^3 (1,040 cm^{-1}) silicate sites. The potential overlap between Si–O SS vibration of Q^2 and the Si–OH stretching mode of silanol groups (970 cm^{-1}) could not be ruled out. Further, the Si–O SS band of Q^3 silicate sites overlapped SS bands of C–O in carbonate groups that appear in the 1,030–1,090 cm^{-1} range for various Na/K/Ca carbonate and bicarbonate phases. The carbonate phases detected in the Na gels were trona and natrite, while that detected in the K gels was potassium carbonate. Trona, natrite, and calcite were observed in the Na-Ca gels. The band assignments of carbonate phases in the Raman spectra were in close agreement with XRD results. The low-frequency range of the Raman data was found to have bands due to the Si–O–Si linkages related to Q^2 (595 cm^{-1}), Q^3 (520–560 cm^{-1}), and Q^4 (445 cm^{-1}) silicate sites for Na and K gels and Q^1 (675 cm^{-1}), Q^3 (560 cm^{-1}), and Q^4 (440 cm^{-1}) silicate sites for Na-Ca gels. In addition, the Na-Ca gels were also observed to have two Q^2 peaks in the low-frequency region, one at 600 cm^{-1} associated to Q^2 silicate sites in Na-Ca gel and the other at 650 cm^{-1} attributed to Q^2 silicate sites in a C-S-H phase.
- Increasing alkali/silica and Ca/Si ratios instigated a progressive depolymerization of the gels, which manifested as gradual shifts in the predominant peaks in the two regions of interest in the Raman spectra. This shift was toward lower wavenumbers in the

high-frequency region and higher wavenumbers in the low-frequency region for Na and K gels with an alkali/silica ratio greater than 0.6. The polymerization trends in the Na-Ca gels were more complex because of the coexistence of a C-S-H phase and Na-Ca gel phase. The specific trends in the silicate polymerization of the gels aligned with published literature on a ^{29}Si MAS NMR spectroscopy on a similar series of synthetic ASR gels.⁽⁴⁶⁾ A strong correlation was observed between the peak position of the most intense band in the low-frequency region (related to Q^3 silicate sites) and the alkali/silica ratio for gels with a composition similar to field ASR gels. Undoubtedly, Raman spectroscopy provides a simple yet powerful method to gain important structural information of amorphous components that could benefit both fundamental research and forensic investigations.

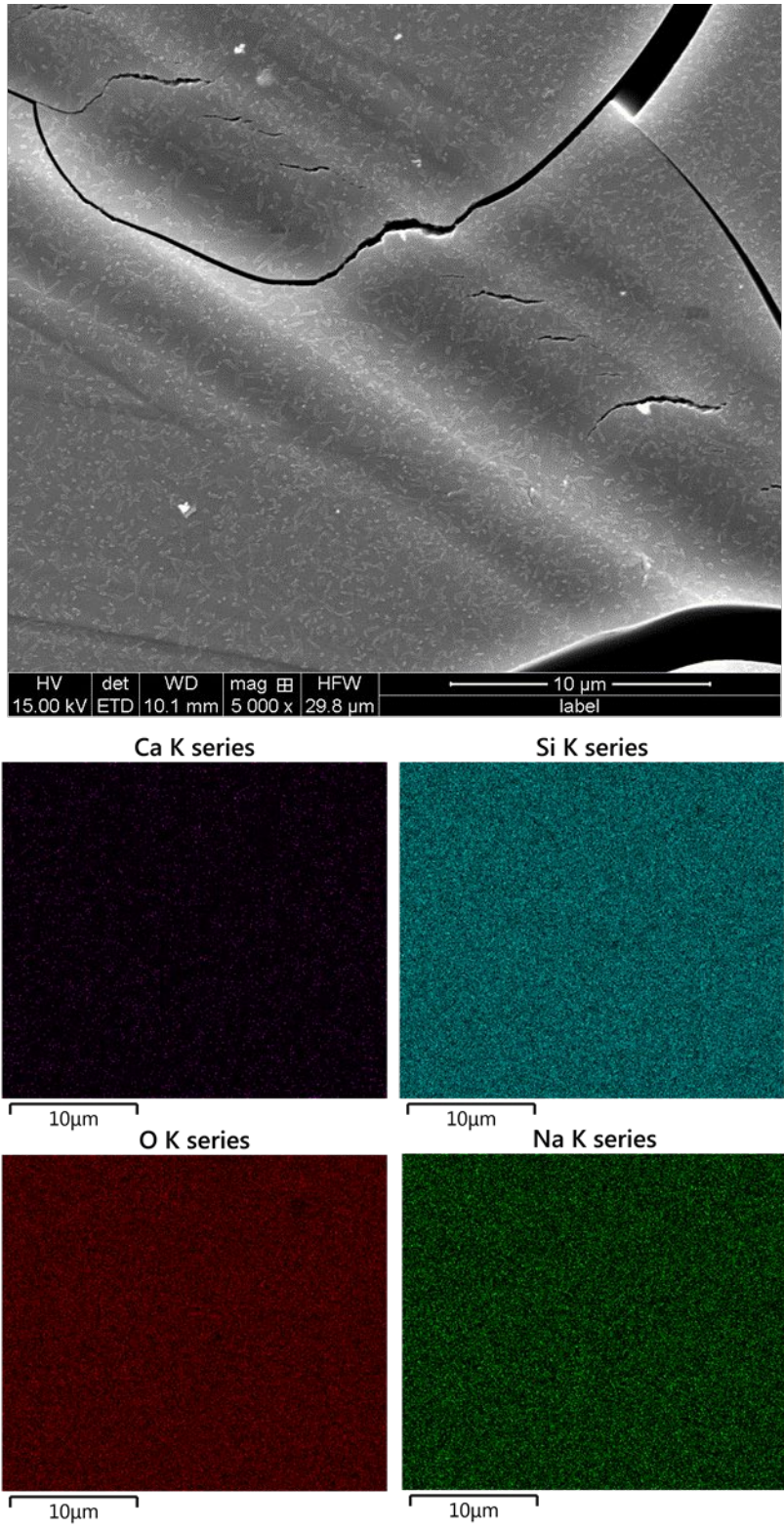
- The Raman spectra of the gels produced in the accelerated ASR samples were collected either in situ from large deposits within voids or extracted from the samples and analyzed on a glass slide. A broad structural interpretation of the Raman spectra suggested that these gels have predominantly Q^2 silicate sites, which may be a result of the aggressively high alkaline environment in which they were produced. In general, the Raman spectroscopic investigation of the gels within cementitious samples demonstrated the immense potential of this technique as a research tool to study ASR gels in field-like samples. However, the application of this technique to ASR-damaged concrete and mortar samples has certain limitations. Obtaining good-quality Raman spectra from samples in early stages of ASR distress or without sizeable amounts of gel may be challenging because the weak Raman signal from the amorphous ASR gels may suffer competition with fluorescence from the cementitious matrix.
- The preliminary data generated from applying SERS to cementitious materials showed promising results that justify further research. The Ag nanoparticles synthesized following Lee and Meisel's method successfully reduced the fluorescence and increased the intensity of the Raman spectra of OPC-paste samples. The enhanced peaks were true peaks, which were confirmed using two different laser wavelengths. The comparison of spectra revealed certain interferences from bands attributed to the Ag nanoparticles in the Raman spectra of cementitious materials. Certain areas in the carbonate stretching, silicate stretching, and silicate bending vibration regions had contribution from Ag nanoparticles. It appeared that the peaks in the Ag nanoparticles may be related to their deposition over the sample. Further, it was observed that, the higher the degree of agglomeration of the Ag nanoparticles, the more intense the peaks were in the Raman spectrum.

Preliminary results suggest that, although there may be some challenges to overcome, there is great potential for successfully developing a SERS technique for analyzing cementitious materials. The research team recommend thoroughly investigating the interaction between the sample and Ag nanoparticles and conducting additional research into variables like the optimal concentration of the suspension based on the nature of the samples before implementing SERS for the routine analysis of cementitious materials. If successful, this technique could be a powerful tool for fundamental research applications and forensic investigations. The research team particularly recommend exploring the application of SERS for improving the sensitivity of

Raman spectroscopy when applied to forensic investigations of concrete deterioration products in close proximity to the cementitious matrix.

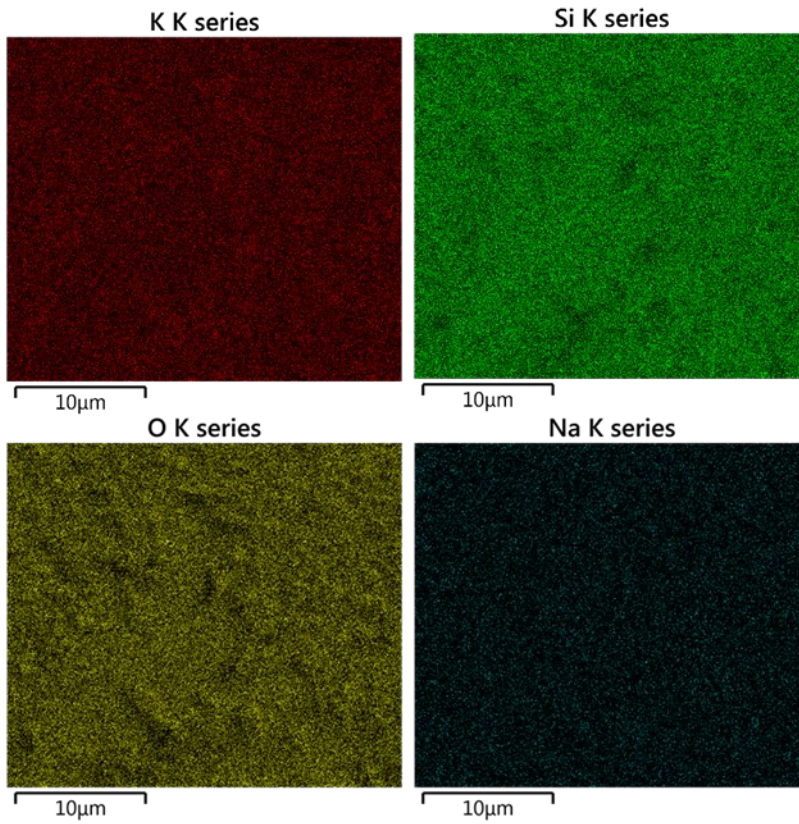
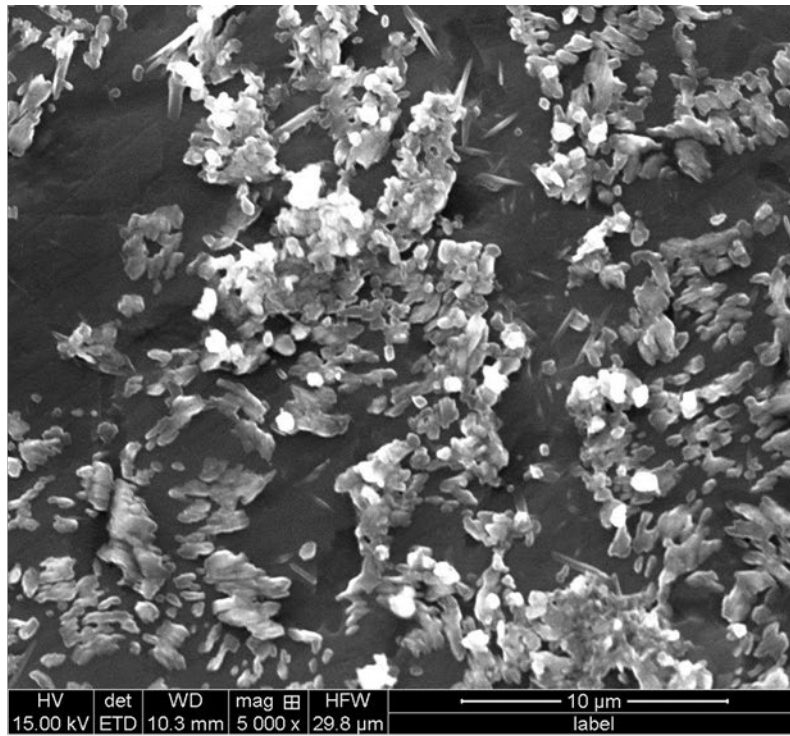
APPENDIX. MORPHOLOGY AND CHEMICAL COMPOSITION OF THE SYNTHETIC ASR GELS

Examples of the morphology and chemical composition, using SEM images and EDS maps, of representative synthetic ASR gels are illustrated in figure 26 through figure 28.



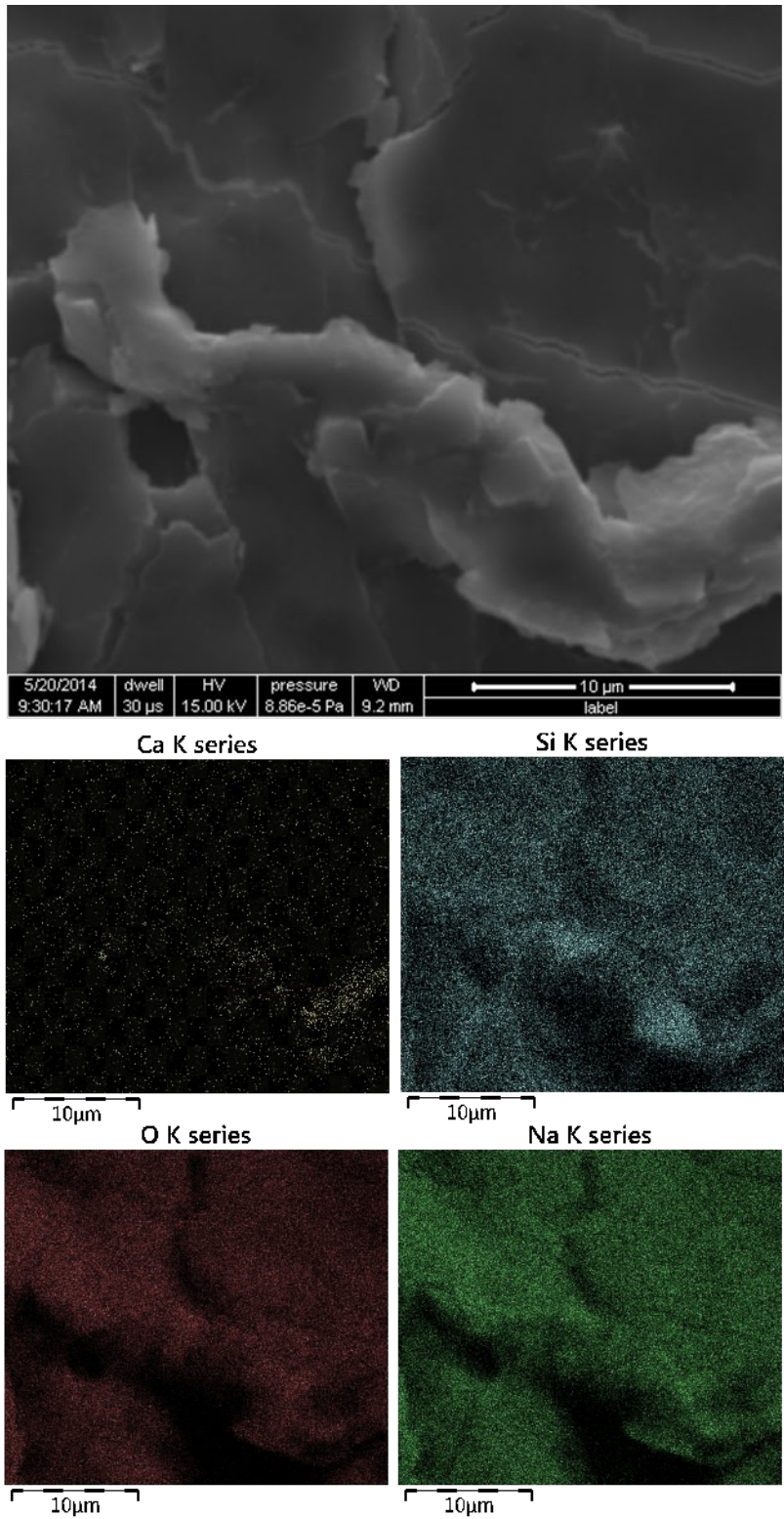
Source: FHWA.

Figure 26. Micrographs. SEM image and EDS elemental maps of NS1 gel.



Source: FHWA.

Figure 27. Micrographs. SEM image and EDS elemental maps of KS2 gel.



Source: FHWA.

Figure 28. Micrographs. SEM image and EDS elemental maps of NCS1 gel.

REFERENCES

1. Thomas, M.D.A., Fournier, B., Folliard, K.J., and Resendez, Y.A. (2011). *Alkali-Silica Reactivity Field Identification Handbook*, Report No. FHWA-HIF-12-022, Federal Highway Administration, Washington, DC.
2. Forster, S.W., Akers, D.J., Lee, M.K., Pergalsky, A., Arrand, C.D., Lewis, D.W., and Boone, R.L. (1998). *State-of-the-Art Report on Alkali-Aggregate Reactivity*, ACI 221.1R-98, American Concrete Institute, Farmington Hills, MI.
3. Ahlstrom, G. (2008). "FHWA Alkali-Silica Reactivity Development and Deployment Program." *HPC Bridge Views*, 51, National Concrete Bridge Council and Federal Highway Administration, Washington, DC.
4. Cooley Jr., L.A. and Brumfield, J.W. (2006). *ASR Benchmark Workshop*.
5. Benmore, C.J. and Monteiro, P.J. (2010). "The structure of alkali silicate gel by total scattering methods." *Cement and Concrete Research*, 40(6), pp. 892–897, Elsevier, Amsterdam, Netherlands.
6. McMillan, P. (1984). "Structural studies of silicate glasses and melts-applications and limitations of Raman spectroscopy." *American Mineralogist*, 69(7-8), pp. 622–644, Mineralogical Society of America, Chantilly, VA.
7. Stanton, T.E. (1940). "Expansion of concrete through reaction between cement and aggregate." *Proceedings of the American Society of Civil Engineers*, 66(10), pp. 1781–1811, American Society of Civil Engineers, Reston, VA.
8. Wustholz, K.L., Brosseau, C.L., Casadio, F., and Van Duyne, R.P. (2009). "Surface-enhanced Raman spectroscopy of dyes: from single molecules to the artists' canvas." *Physical Chemistry Chemical Physics*, 11, pp. 7350–7359, Royal Society of Chemistry, London, UK.
9. Liu, C., Wang, S., Chen, G., Xu, S., Jia, Q., Zhou, J., and Xu, W. (2014). "A surface-enhanced Raman scattering (SERS)-active optical fiber sensor based on a three-dimensional sensing layer." *Sensing and Biosensing Research*, 1, pp. 8–14, Elsevier, Amsterdam, Netherlands.
10. Bensted, J. (1976). "Uses of Raman spectroscopy in cement chemistry." *Journal of the American Ceramic Society*, 59(3-4), pp. 140–143, John Wiley & Sons, Hoboken, NJ.
11. Bensted, J. and Varma, S. (1977). "Infrared and Raman spectroscopy in cement chemistry--miscellaneous applications." *World Cement Technology*, 8(1), p. 16, Cement and Concrete Association, London, UK.

12. Martínez-Ramírez, S. and Fernández-Carrasco, L. (2011). “Raman spectroscopy: Application to cementitious systems.” *Construction and Building: Design, Materials, and Techniques*, pp. 233–244, Ed. S.G. Doyle, Nova Science Publishers, New York, NY.
13. Black, L. (2011). “Raman spectroscopy of cements: Problems and possibilities.” *Proceedings of 13th Euroseminar of Microscopy Applied to Building Materials (EMABM)*, pp. 6–7, White Rose Research Online, Ljubljana, Slovenia. Available online: http://eprints.whiterose.ac.uk/43102/7/Black16_front.pdf, last accessed April 4, 2019.
14. Potgieter-Vermaak, S.S., Potgieter, J.H., and Van Grieken, R. (2006). “The application of Raman spectrometry to investigate and characterize cement, Part I: A review.” *Cement and concrete research*, 36(4), pp. 656–662, Elsevier, Amsterdam, Netherlands.
15. Skibsted, J. and Hall, C. (2008). “Characterization of cement minerals, cements and their reaction products at the atomic and nano scale.” *Cement and Concrete Research*, 38(2), pp. 205–225, Elsevier, Amsterdam, Netherlands.
16. Richardson, I.G., Skibsted, J., Black, L., and Kirkpatrick, R.J. (2010). “Characterisation of cement hydrate phases by TEM, NMR and Raman spectroscopy.” *Advances in Cement Research*, 22(4), pp. 233–248, ICE Publishing, London, UK.
17. Conjeaud, M. and Boyer, H. (1980). “Some possibilities of Raman microprobe in cement chemistry.” *Cement and Concrete Research*, 10(1980), pp. 61–70, Elsevier, Amsterdam, Netherlands.
18. Dyer, C.D., Hendra, P.J., and Forsling, W. (1993). “The Raman spectroscopy of cement minerals under 1064 nm excitation.” *Spectrochimica Acta Part A: Molecular Spectroscopy*, 49(5–6), pp. 715–722, Elsevier, Amsterdam, Netherlands.
19. Newman, S.P., Clifford, S.J., Coveney, P.V., Gupta, V., Blanchard, J.D., Serafin, F., and Diamond, S. (2005). “Anomalous fluorescence in near-infrared Raman spectroscopy of cementitious materials.” *Cement and Concrete Research*, 35(8), pp. 1620–1628, Elsevier, Amsterdam, Netherlands.
20. Black, L. (2009). “Raman spectroscopy of cementitious materials.” *Spectroscopic Properties of Inorganic and Organometallic Compounds: Techniques, Materials and Applications*, 40, Eds. J. Yarwood, R. Douthwaite, and S. Duckett, Royal Society of Chemistry, London, UK.
21. Gastaldi, D., Boccaleri, E., and Canonico, F. (2008). “In situ Raman study of mineral phases formed as by-products in a rotary kiln for clinker production.” *Journal of Raman Spectroscopy*, 39(7), pp. 806–812, John Wiley & Sons, Hoboken, NJ.
22. Black, L. and Brooker, A. (2007). “SEM–SCA: combined SEM–Raman spectrometer for analysis of OPC clinker.” *Advances in Applied Ceramics*, 106(6), pp. 327–334, Taylor and Francis, Oxfordshire, UK.

23. Ibáñez, J., Artús, L., Cuscó, R., López, Á., Menéndez, E., and Andrade, M.C. (2007). “Hydration and carbonation of monoclinic C2S and C3S studied by Raman spectroscopy.” *Journal of Raman Spectroscopy*, 38(1), pp. 61–67, John Wiley & Sons, Hoboken, NJ.
24. Tarrida, M., Madon, M., Le Rolland, B., and Colombet, P. (1995). “An in-situ Raman spectroscopy study of the hydration of tricalcium silicate.” *Advanced Cement Based Materials*, 2(1), pp. 15–20, Pergamon Press, Oxford, UK.
25. Black, L., Breen, C., Yarwood, J., Deng, C.S., Phipps, J., and Maitland, G. (2006). “Hydration of tricalcium aluminate (C 3 A) in the presence and absence of gypsum—studied by Raman spectroscopy and X-ray diffraction.” *Journal of Materials Chemistry*, 16(13), pp. 1263–1272, Royal Society of Chemistry, London, UK.
26. Li, J., Yu, Q., Wei, J., and Zhang, T. (2011). “Structural characteristics and hydration kinetics of modified steel slag.” *Cement and Concrete Research*, 41(3), pp. 324–329, Elsevier, Amsterdam, Netherlands.
27. Higl, J., Köhler, M., and Lindén, M. (2016). “Confocal Raman microscopy as a non-destructive tool to study microstructure of hydrating cementitious materials.” *Cement and Concrete Research*, 88, pp. 136–143, Elsevier, Amsterdam, Netherlands.
28. Torres-Carrasco, M., del Campo, A., de la Rubia, M.A., Reyes, E., Moragues, A., and Fernández, J.F. (2017). “Confocal Raman Microscopy: new perspective on the weathering of anhydrous cement.” *IOP Conference Series: Materials Science and Engineering*, 251(1), IOP Publishing, Bristol, UK.
29. Renaudin, G., Segni, R., Mentel, D., Nedelec, J.M., Leroux, F., and Taviot-Gueho, C. (2007). “A Raman study of the sulfated cement hydrates: ettringite and monosulfoaluminate.” *Journal of Advanced Concrete Technology*, 5(3), pp. 299–312, Japan Concrete Institute, Tokyo, Japan.
30. Garg, N., Wang, K., and Martin, S.W. (2013). “A Raman spectroscopic study of the evolution of sulfates and hydroxides in cement–fly ash pastes.” *Cement and Concrete Research*, 53, pp. 91–103, Elsevier, Amsterdam, Netherlands.
31. Brough, A.R. and Atkinson, A. (2001). “Micro-Raman spectroscopy of thaumasite.” *Cement and Concrete Research*, 31(3), pp. 421–424, Elsevier, Amsterdam, Netherlands.
32. Jallad, K.N., Santhanam, M., Cohen, M.D., and Ben-Amotz, D. (2001). “Chemical mapping of thaumasite formed in sulfate-attacked cement mortar using near-infrared Raman imaging microscopy.” *Cement and Concrete Research*, 31(6), pp. 953–958, Elsevier, Amsterdam, Netherlands.
33. Yue, Y., Bai, Y., Basheer, P.M., Boland, J.J., and Wang, J.J. (2013). “Monitoring the cementitious materials subjected to sulfate attack with optical fiber excitation Raman spectroscopy.” *Optical Engineering*, 52(10), Society of Photo-Optical Instrumentation Engineers, Bellingham, WA.

34. Black, L., Breen, C., Yarwood, J., Garbev, K., Stemmermann, P., and Gasharova, B. (2007). “Structural features of C–S–H (I) and its carbonation in air—a Raman spectroscopic study. Part II: carbonated phases.” *Journal of the American Ceramic Society*, 90(3), pp. 908–917, John Wiley & Sons, Hoboken, NJ.
35. El-Turki, A., Ball, R. J., and Allen, G.C. (2007). “The influence of relative humidity on structural and chemical changes during carbonation of hydraulic lime.” *Cement and Concrete Research*, 8(37), pp. 1233–1240, Elsevier, Amsterdam, Netherlands.
36. Martinez-Ramirez, S., Sanchez-Cortes, S., Garcia-Ramos, J.V., Domingo, C., Fortes, C., and Blanco-Varela, M.T. (2003). “Micro-Raman spectroscopy applied to depth profiles of carbonates formed in lime mortar.” *Cement and Concrete Research*, 33(12), pp. 2063–2068, Elsevier, Amsterdam, Netherlands.
37. Aguiar, H. Serra, J., González, P., and León, B. (2009). “Structural study of sol–gel silicate glasses by IR and Raman spectroscopies.” *Journal of Non-Crystalline Solids*, 355(8), pp. 475–480, Elsevier, Amsterdam, Netherlands.
38. Malfait, W.J., Zakaznova-Herzog, V.P., and Halter, W.E. (2008). “Amorphous materials: Properties, structure, and durability: Quantitative Raman spectroscopy: Speciation of Na-silicate glasses and melts.” *American Mineralogist*, 93(10), pp. 1505–1518, Mineralogical Society of America, Chantilly, VA.
39. Zakaznova-Herzog, V.P., Malfait, W.J., Herzog, F., and Halter, W.E. (2007). “Quantitative Raman spectroscopy: Principles and application to potassium silicate glasses.” *Journal of Non-Crystalline Solids*, 353(44–46), pp. 4015–4028, Elsevier, Amsterdam, Netherlands.
40. Kirkpatrick, R.J., Yarger, J.L., McMillan, P.F., Ping, Y., and Cong, X. (1997). “Raman spectroscopy of CSH, tobermorite, and jennite.” *Advanced Cement Based Materials*, 5(3–4), pp. 93–99, Pergamon Press, Oxford, UK.
41. Garbev, K., Stemmermann, P., Black, L., Breen, C., Yarwood, J., and Gasharova, B. (2007). “Structural features of C–S–H (I) and its carbonation in air—a Raman spectroscopic study. Part I: fresh phases.” *Journal of the American Ceramic Society*, 90(3), pp. 900–907, John Wiley & Sons, Hoboken, NJ.
42. Martinez-Ramirez, S., Frías, M., and Domingo, C. (2006). “Micro-Raman spectroscopy in white portland cement hydration: long-term study at room temperature.” *Journal of Raman Spectroscopy*, 37(5), pp. 555–561, John Wiley & Sons, Hoboken, NJ.
43. Balachandran, C., Muñoz, J.F., and Arnold, T. (2017). “Characterization of alkali silica reaction gels using Raman spectroscopy.” *Cement and Concrete Research*, 92, pp. 66–74, Elsevier, Amsterdam, Netherlands.
44. Balachandran, C., Munoz, J.F., Arnold, T., and Youtcheff, J. (2015). “Potential Application of Surface Enhanced Raman Spectroscopy as a Tool to Study Cementitious Materials.” *Nanotechnology in Construction*, Eds. K. Sobolev and S.P. Shah, pp. 93–98, Springer, Cham, Switzerland.

45. Leemann, A. (2017). "Raman microscopy of alkali-silica reaction (ASR) products formed in concrete." *Cement and Concrete Research*, 102, pp. 41–47, Elsevier, Amsterdam, Netherlands.
46. Hou, X., Kirkpatrick, R.J., Struble, L.J., and Monteiro, P.J. (2005). "Structural investigations of alkali silicate gels." *Journal of the American Ceramic Society*, 88(4), pp. 943–949, John Wiley & Sons, Hoboken, NJ.
47. Benmore, C.J. and Monteiro, P.J. (2010). "The structure of alkali silicate gel by total scattering methods." *Cement and Concrete Research*, 40(6), pp. 892–897, Elsevier, Amsterdam, Netherlands.
48. Potgieter-Vermaak, S.S., Potgieter, J.H., Belleil, M., DeWeerd, F., and Van Grieken, R. (2006). "The application of Raman spectrometry to the investigation of cement: Part II: A micro-Raman study of OPC, slag and fly ash." *Cement and Concrete Research*, 36(4), pp. 663–670, Elsevier, Amsterdam, Netherlands.
49. Deng, C.S., Breen, C., Yarwood, J., Habesch, S., Phipps, J., Craster, B., and Maitland, G. (2002). "Ageing of oilfield cement at high humidity: a combined FEG-ESEM and Raman microscopic investigation." *Journal of Materials Chemistry*, 12(10), pp. 3105–3112, Royal Society of Chemistry, London, UK.
50. Kumar, G.V. (2012). "Plasmonic nano-architectures for surface enhanced Raman scattering: a review." *Journal of Nanophotonics*, 6(1), Society of Photo-Optical Instrumentation Engineers, Bellingham, WA.
51. Muniz-Miranda, M., Gellini, C., and Innocenti, M. (2012). "SERS Spectroscopy and Microscopy." *Raman Spectroscopy for Nanomaterials Characterization*, Ed. C. Kumar, pp. 553–586, Springer, Berlin, Germany.
52. Kneipp, K., Wang, Y., Kneipp, H., Perelman, L.T., Itzkan, I., Dasari, R.R., and Feld, M.S. (1997). "Single molecule detection using surface-enhanced Raman scattering (SERS)." *Physical Review Letters*, 78(9), p. 1667, American Physical Society, College Park, MD.
53. Kneipp, K., Kneipp, H., Deinum, G., Itzkan, I., Dasari, R.R., and Feld, M. S. (1998). "Single-molecule detection of a cyanine dye in silver colloidal solution using near-infrared surface-enhanced Raman scattering." *Applied Spectroscopy*, 52(2), pp. 175–178, SAGE Publishing, Washington, DC.
54. Shi, X., Ma, J., Zheng, R., Wang, C., and Kronfeldt, H.D. (2012). "An improved self-assembly gold colloid film as surface-enhanced Raman substrate for detection of trace-level polycyclic aromatic hydrocarbons in aqueous solution." *Journal of Raman Spectroscopy*, 43(10), pp. 1354–1359, John Wiley & Sons, Hoboken, NJ.
55. Olea-Mejía, O., Fernández-Mondragón, M., Rodríguez-de la Concha, G., and Camacho-López, M. (2015). "SERS-active Ag, Au and Ag–Au alloy nanoparticles obtained by laser ablation in liquids for sensing methylene blue." *Applied Surface Science*, 348, pp. 66–70, Elsevier, Amsterdam, Netherlands.

56. Chen, K., Vo-Dinh, K.C., Yan, F., Wabuyele, M.B., and Vo-Dinh, T. (2006). "Direct identification of alizarin and lac dye on painting fragments using surface-enhanced Raman scattering." *Analytica Chimica Acta*, 569(1–2), pp. 234–237, Elsevier, Amsterdam, Netherlands.
57. Centeno, S.A. and Shamir, J. (2008). "Surface enhanced Raman scattering (SERS) and FTIR characterization of the sepia melanin pigment used in works of art." *Journal of Molecular Structure*, 873(1–3), pp. 149–159, Elsevier, Amsterdam, Netherlands.
58. Muniz-Miranda, M., Gellini, C., and Bindl, L. (2009). "Surface-enhanced Raman spectroscopy for identifying rock composition." *Spectrochimica Acta Part A: Molecular and Biomolecular Spectroscopy*, 73(3), pp. 456–459, Elsevier, Amsterdam, Netherlands.
59. Schlegel, V.L., and Cotton, T.M. (1991). "Silver-island films as substrates for enhanced Raman scattering: effect of deposition rate on intensity." *Analytical Chemistry*, 63(3), pp. 241–247, American Chemical Society, Washington, DC.
60. Whitney, A.V., Van Duyne, R.P., and Casadio, F. (2006). "An innovative surface-enhanced Raman spectroscopy (SERS) method for the identification of six historical red lakes and dyestuffs." *Journal of Raman Spectroscopy*, 37(10), pp. 993–1002, John Wiley & Sons, Hoboken, NJ.
61. Abalde-Cela, S., Ho, S., Rodríguez-González, B., Correa-Duarte, M.A., Álvarez-Puebla, R.A., Liz-Marzán, L.M., and Kotov, N.A. (2009). "Loading of exponentially grown LBL films with silver nanoparticles and their application to generalized SERS detection." *Angewandte Chemie International Edition*, 48(29), pp. 5326–5329, John Wiley & Sons, Hoboken, NJ.
62. Wustholz, K.L., Brosseau, C.L., Casadio, F., and Van Duyne, R.P. (2009). "Surface-enhanced Raman spectroscopy of dyes: from single molecules to the artists' canvas." *Physical Chemistry Chemical Physics*, 11(34), pp. 7350–7359, Royal Society of Chemistry, London, UK.
63. Liu, C., Wang, S., Chen, G., Xu, S., Jia, Q., Zhou, J., and Xu, W. (2014). "A surface-enhanced Raman scattering (SERS)-active optical fiber sensor based on a three-dimensional sensing layer." *Sensing and Bio-Sensing Research*, 1, pp. 8–14, Elsevier, Amsterdam, Netherlands.
64. Struble, L.J. (1979). "Chapter 2. Experimental Methods." *Swell and other properties of synthetic alkali-silica gels*, Master's thesis, pp. 10–16, Purdue University, West Lafayette, IN.
65. Ostertag, C.P., Yi, C., and Monteiro, P.J. (2007). "Effect of confinement on properties and characteristics of alkali-silica reaction gel." *ACI Materials Journal*, 104(3), p. 276, American Concrete Institute, Farmington Hills, MI.

66. ASTM International. (2007a). *Standard test method for concrete aggregates by determination of length change of concrete due to alkali-silica reaction*, C1293, ASTM International, West Conshohocken, PA.
67. ASTM International. (2007b). *Standard test method for potential alkali reactivity of aggregates (Mortar-Bar method)*, C1260, ASTM International, West Conshohocken, PA.
68. Lee, P.C. and Meisel, D. (1982). "Adsorption and surface-enhanced Raman of dyes on silver and gold sols." *The Journal of Physical Chemistry*, 86(17), pp. 3391–3395, American Chemical Society, Washington, DC.
69. Mysen, B.O., Finger, L.W., Virgo, D., and Seifert, F.A. (1982). "Curve-fitting of Raman spectra of silicate glasses." *American Mineralogist*, 67(7-8), pp. 686–695, Mineralogical Society of America, Chantilly, VA.
70. McMillan, P. and Piriou, B. (1983). "Raman spectroscopic studies of silicate and related glass structure: a review." *Bulletin de Minéralogie*, 106(1-2), pp. 57–75, Masson Éditeur, Paris, France.
71. McMillan, P. (1984). "A Raman spectroscopic study of glasses in the system CaO-MgO-SiO₂." *American Mineralogist*, 69(7-8), pp. 645–659, Mineralogical Society of America, Chantilly, VA.
72. Neuville, D.R. and Mysen, B.O. (1996). "Role of aluminium in the silicate network: In situ, high-temperature study of glasses and melts on the join SiO₂-NaAlO₂." *Geochimica et Cosmochimica Acta*, 60(10), pp. 1727–1737, Elsevier, Amsterdam, Netherlands.
73. Liem, N.Q., Sagon, G., Quang, V.X., Tan, H.V., and Colomban, P. (2000). "Raman study of the microstructure, composition and processing of ancient Vietnamese (proto) porcelains and celadons (13-16th centuries)." *Journal of Raman Spectroscopy*, 31(10), pp. 933–942, John Wiley & Sons, Hoboken, NJ.
74. Hou, X., Struble, L.J., and Kirkpatrick, R.J. (2004). "Formation of ASR gel and the roles of CSH and portlandite." *Cement and Concrete Research*, 34(9), pp. 1683–1696, Elsevier, Amsterdam, Netherlands.
75. Kim, T. and Olek, J. (2012). "Effects of Sample Preparation and Interpretation of Thermogravimetric Curves on Calcium Hydroxide in Hydrated Pastes and Mortars." *Transportation Research Record*, 2290(1), pp. 10–18, National Research Council, Washington, DC.
76. Newbury, D.E. and Ritchie, N.W.M. (2014). "Performing elemental microanalysis with high accuracy and high precision by scanning electron microscopy/silicon drift detector energy-dispersive X-ray spectrometry (SEM/SDD-EDS)." *Journal of Materials Science*, 50, pp. 493–518, Kluwer Academic Publishers, Dordrecht, Netherlands.

77. Rossen, J.E. and Scrivener, K.L. (2017). “Optimization of SEM-EDS to determine the C–A–S–H composition in matured cement paste samples.” *Materials Characterization*, 123, pp. 294–306, Elsevier, Amsterdam, Netherlands.
78. Kamitsos, E.I., Kapoutsis, J.A., Jain, H., and Hsieh, C.H. (1994). “Vibrational study of the role of trivalent ions in sodium trisilicate glass.” *Journal of Non-Crystalline Solids*, 171(1), pp. 31–45, Elsevier, Amsterdam, Netherlands.
79. Matson, D.W., Sharma, S.K., and Philpotts, J.A. (1983). “The structure of high-silica alkali-silicate glasses. A Raman spectroscopic investigation.” *Journal of Non-Crystalline Solids*, 58(2–3), pp. 323–352, Elsevier, Amsterdam, Netherlands.
80. McMillan, P.F. and Remmele, R.L. (1986). “Hydroxyl sites in SiO₂ glass: A note on infrared and Raman spectra.” *American Mineralogist*, 71(5-6), pp. 772–778, Mineralogical Society of America, Chantilly, VA.
81. Lafuente, B., Downs, R.T., Yang, H., and Stone, N. (2016). “The power of databases: the RRUFF project.” *Highlights in mineralogical crystallography*, Eds. T. Armbruster and R.M. Danisi, pp. 1–29, Walter de Gruyter GmbH.
82. Buzgar, N. and Apopei, A.I. (2009). “The Raman study of certain carbonates.” *Analele Stiintifice de Universitatii AI Cuza din Iasi. Sect. 2, Geologie*, 55(2), p. 97, Universitatea Alexandru Ioan Cuza din Iași, Iași, Romania.
83. Garnica-Romo, M.G., Yañez-Limón, J.M., Villicana, M., Pérez-Robles, J.F., Zamorano-Ulloa, R., and González-Hernandez, J. (2004). “Structural evolution of sol–gel SiO₂ heated glasses containing silver particles.” *Journal of Physics and Chemistry of Solids*, 65(6), pp. 1045–1052, Elsevier, Amsterdam, Netherlands.
84. Yu, P., Kirkpatrick, R.J., Poe, B., McMillan, P.F., and Cong, X. (1999). “Structure of calcium silicate hydrate (C-S-H): Near-, Mid-, and Far-infrared spectroscopy.” *Journal of the American Ceramic Society*, 82(3), pp. 742–748, John Wiley & Sons, Hoboken, NJ.
85. Sinko, K., Mezei, R., Rohonczy, J., and Fratzl, P. (1999). “Gel structures containing Al(III).” *Langmuir*, 15(20), pp. 6631–6636, American Chemical Society, Washington, DC.
86. Tambelli, C.E., Schneider, J.F., Hasparyk, N.P., and Monteiro, P.J.M. (2006). “Study of the structure of alkali–silica reaction gel by high-resolution NMR spectroscopy.” *Journal of Non-Crystalline Solids*, 352(32–35), pp. 3429–3436, Elsevier, Amsterdam, Netherlands.
87. Cong, X.D., Kirkpatrick, R.J., and Diamond, S. (1993). “²⁹Si MAS NMR spectroscopic investigation of alkali silica reaction product gels.” *Cement and Concrete Research*, 23(4), pp. 811–823, Elsevier, Amsterdam, Netherlands.
88. Leemann, A., Le Saout, G., Winnefeld, F., Rentsch, D., and Lothenbach, B. (2011). “Alkali–silica reaction: the influence of calcium on silica dissolution and the formation of reaction products.” *Journal of the American Ceramic Society*, 94(4), pp. 1243–1249, John Wiley & Sons, Hoboken, NJ.

89. Tian, Z., Ren, B., Li, J., and Yang, Z. (2007). “Expanding generality of surface-enhanced Raman spectroscopy with borrowing SERS activity strategy.” *Chemical Communications*, 34, pp. 3514–3534, Royal Society of Chemistry, London, UK.
90. Sánchez-Cortés, S. and García-Ramos, J.V. (1998). “Anomalous Raman bands appearing in surface-enhanced Raman spectra.” *Journal of Raman Spectroscopy*, 29(5), pp. 365–371, John Wiley & Sons, Hoboken, NJ.

